Microstructural Peculiarities of Al-Rich Al-La-Ni-Fe Alloys

A.L. VASILIEV, N.D. BAKHTEEVA, M.YU. PRESNIAKOV, S. LOPATIN,
N.N. KOLOBYLINA, A.G. IVANOVA, and E.V. TODOROVA

The results of a comprehensive microstructural study of the ternary and quaternary phases in air-cast $Al_{85}Ni_{11-x}Fe_xLa_4$ (where $x = 2$ and 4 at. pct) polycrystalline alloys by means of optical microscopy, scanning electron microscopy, transmission electron microscopy, scanning transmission electron microscopy, energy-dispersive X-ray microanalysis, and X-ray diffraction are presented. It was found that these alloys contain several phases, namely, fcc-Al, $Al_{11}La_3$, $Al_3Ni_{1-x}Fe_x$, $Al_9Ni_{2-x}Fe_x$, $Al_8Fe_{2-x}Ni_xLa$, and $Al_{3.2}Fe_{1-x}Ni_x$, in the form of δ-layers in $Al_8Fe_{2-x}Ni_xLa$ particles. A high density of other defects in the quaternary $Al_8Fe_{2-x}Ni_xLa$ particles was found, and the formation of these defects could be caused by the dendritic type of growth of this phase. The crystal structures of all these defects were revealed by high-resolution scanning transmission electron microscopy together with atomic-resolution energy-dispersive X-ray microanalysis. The thermal stability of the ternary and quaternary phases was also studied. The $Al_8Fe_{2-x}Ni_xLa$ phase is metastable and undergoes an irreversible transformation: $Al_8Fe_{2-x}Ni_xLa \rightarrow Al_9Ni_{2-x}Fe_x + Al_{11}La_3$. Based on these data, a sequence of solid-phase reactions in these alloys during cooling and heating is proposed.

https://doi.org/10.1007/s11661-019-05127-x

I. INTRODUCTION

SINCE the seeding studies of Inoue *et al.*[1,2] and G. Shiflet *et al.*[3] in 1988, Al-based metal glasses containing rare-earth elements (RE) together with transition metals (TM) have been under intensive study due to their high metallic glass formation ability and excellent mechanical properties, such as high strength and corrosion resistance. Two groups of ternary Al-based alloys containing La, namely, Al-La-Ni and Al-La-Fe, were already considered in those pioneering research works. In subsequent studies, it was shown that the reported high glass-forming ability and mechanical properties could be substantially improved by the addition of a second transition element.[4–6] The quaternary alloys with two transition elements, in particular Fe and Ni, are characterized by a higher thermal stability and better mechanical properties. Studies of the microstructure and phase formation processes in ternary and quaternary alloys during annealing have been carried out mainly by X-ray and electron diffraction (XRD and ED, respectively) since these materials were discovered, but in most cases, they were limited to ascertaining the presence of fcc-Al and one or more binary phases. Quaternary intermetallic compounds, to the best of our knowledge, were not found and were not considered. To some extent, this might be due to issues related to the completeness of their identification by XRD or ED for a number of reasons. On the one hand, XRD spectra from low-symmetry binary phases exhibit a significant number of maxima, which could conceal the presence of ternary and quaternary phases.

Studies of the microstructure of amorphous alloys after thermal treatment or intense plastic deformation were carried out mostly in samples with extremely high mechanical characteristics in which the grain sizes often did not exceed 100 nm.[4,7,8] Such grain sizes precluded investigations by ED; however, these alloys are most interesting. In addition, during annealing or intensive plastic deformation, along with stable phases, metastable intermetallic phases could appear. If so, for

---

A.L. VASILIEV is with the National Research Center "Kurchatov Institute", Ak. Kurchatov sq. 1, 123182 Moscow, Russia, with the Shubnikov Institute of Crystallography of FSRC "Crystallography and Photonics", RAS, Leninsky pr, 59, 119333 Moscow, Russia, and also with Moscow Institute of Physics and Technology, 9 Institutskiy per., Dolgoprudny, 141701 Moscow Region, Russia. Contact e-mail: a.vasiliev56@gmail.com N.D. BAKHTEEVA and E.V. TODOROVA are with the Baikov Institute of Metallurgy and Materials Science, RAS, Leninsky pr, 39, 119334 Moscow, Russia. M.YU. PRESNIAKOV and N.N. KOLOBYLINA are with the National Research Center "Kurchatov Institute". S. LOPATIN is with the King Abdullah University of Science and Technology (KAUST), Core Labs, Thuwal, 23955-6900, Saudi Arabia. A.G. IVANOVA is with the Shubnikov Institute of Crystallography of FSRC "Crystallography and Photonics".

Manuscript submitted May 23, 2018.

an unambiguous interpretation of the XRD spectra, ED patterns and phase determination, a comprehensive study of polycrystalline alloys is necessary, as previously reported.[9,10,11,12] A possible phase composition of the alloys can be determined from phase diagrams, but quaternary Al-La-Ni-Fe alloys have been insufficiently studied, and the necessary phase diagrams were not found in the literature. The ternary phase diagrams of the Al-Fe-La system[13,14] and the Al-La-Ni system[15,16] have been previously presented. The Al-Ni-Fe system has been studied more thoroughly, and the phase diagrams for several isothermal sections were described by Rivlin[17] and updated later in papers[18] by Khaidar *et al.*,[19] as well as in the relatively recent works of Budberg *et al.*,[20] Raghavan,[21] Eleno *et al.*,[22] Chumak *et al.*[23] and Zhang *et al.*[24,25,26]

Table I summarizes the known intermetallic phases in the Al-Ni-Fe-La system with Al ≥ 70 at. pct. These alloys contain polycrystalline fcc-Al and several binary and ternary phases. Two Al-Ni binary phases are known in this Al concentration range: the first one is Al_3Ni,[27] and the second one is Al_9Ni_2.[28] It is assumed that the Al_3Ni phase has a very narrow homogeneity range.[29] Eleno and co-workers [22] defined this range as ~ 23 to 26 at. pct Ni. Yamamoto and Tsubakino[28] determined by ED the Al_9Ni_2 phase, which is isostructural to Al_9Co_2 and turned out to be metastable. Moreover, according to the energy-dispersive X-ray (EDX) microanalysis, the Al content in the Al_9Ni_2 particles was above the stoichiometric Al/Ni atomic ratio of 4.68. Four basic binary Al-Fe intermetallic phases with different crystal structures and stoichiometries with Al contents above 70 at. pct were discovered. The Al_5Fe_2 phase exhibits an orthorhombic crystal structure (space group (*SG) Cmcm*).[30,31] This compound is isomorphic with the hexagonal compound Al_5Co_2[32] and has a homogeneity range of 70 to 73 at. pct Al.[22] The group of Al_3Fe, $Al_{13}Fe_4$, $Al_{3.2}Fe$, and $Al_{9.75}Fe_3$ is characterized by a monoclinic crystal structure with very close unit cell parameters. The homogeneity range is 74.5 to 76.6 at. pct Al.[22] Several isostructural compounds with slight differences in the stoichiometric composition have been investigated (see Table I, the structure parameters are given according to the first reference). A phase designated as Al_9Fe_2 was found by ED in the ternary AI-Fe-Si system (A1-0.5 Fe-0.2 Si wt pct alloy)[33]; it was isostructural with Al_9Co_2 and was shown to be monoclinic with lattice parameters $a = 0.869$ nm, $b = 0.635$ nm, $c = 0.632$ nm, and $\beta = 93.4$ deg. In other studies, it was not detected and so can be regarded as metastable. Another metastable phase, Al_6Fe, was first described by Hollingworth *et al.*[34] and later refined.[35] The homogeneity ranges of the last two phases remain undefined.

Three stable Al-Fe-Ni ternary phases with Al ≥ 70 at. pct (displayed in the order of increasing Al content in Table I) were found: 1—quasi-crystalline $Al_{71}Fe_5Ni_{24}$, 2—hexagonal with the general formula $Al_{10}Fe_{4\text{-}x}Ni_x$, and 3—monoclinic $Al_9Fe_{2\text{-}x}Ni_x$. The last two phases are denoted by τ_1 and τ_2, and different authors, for example References 17 and 23, use the opposite notation. The $Al_{10}Fe_{4-x}Ni_x$ and $Al_9Fe_{2-x}Ni_x$ phases were first described in the investigation of Bradley and Taylor,[36] where they were claimed to be isostructural with Al_5Co_2 and Al_9Co_2, respectively. Schroder and Hanemann[37] shortly afterwards determined the homogeneity ranges of these compounds: for $Al_{10}Fe_3Ni$, the range of Fe was 18 to 24.5 at. pct and the range of Ni was 4.5 to 10.5 at pct; for Al_9FeNi, Fe was in the range of 4.4 to 11.1 at. pct and Ni was in the range of 7.0 to 13.5 at. pct. Later, the structures, compositions and homogeneity ranges of compounds with the general formulas $Al_{10}Fe_{4-x}Ni_x$ and $Al_9Fe_{2-x}Ni_x$ were critically evaluated by Mondolfo[38] and Rivlin[17] with amendments in their later study,[18] as well as by Raghavan,[39] Dubko,[29] and Budberg *et al.*,[20] and updated by Raghavan,[21] Eleno *et al.*,[22] Chumak *et al.*,[23] and Zhang *et al.*[25] Based on these studies, the homogeneity ranges can be extended: for $Al_{10}Fe_{4\text{-}x}Ni_x$, Fe is in the range of 14.4 to 24.5 at. pct and Ni is in the range of 4.5 to 13.1 at. pct. For the $Al_9Fe_{2-x}Ni_x$ phase, the range for Fe is 3.05 to 11.1 at. pct and the range for Ni is 4.5 to 14.3 at. pct. According to Chumak and co-workers,[23] the Al atoms at the 2α site can be substituted by Fe/Ni atoms in $Al_{10}Fe_{4-x}Ni_x$. The ab = 0.629 nm, c = 0.621 nmove homogeneity range for $Al_{10}Fe_{4-x}Ni_x$ includes $Al_{10}Fe_3Ni$, determined by Reference 40 and confirmed by Khaidar and co-workers,[19] and Al_5FeNi, discovered by Ellner and Rohrer.[41] However, the composition of $Al_{10}FeNi_3$ mentioned by Khaidar *et al.*[19] does not fit this homogeneity region. This paper reported that the particle size of the polycrystalline alloy was too small to determine its structure. This phase was not found in later studies, and that was the reason for its absence in Table I. In a number of studies,[19,29,37] it was noted that the $Al_9Fe_{2-x}Ni_x$ phase was formed *via* the peritectic reaction L + $Al_{13}Fe4$ + Al_3Ni ↔ $Al_9Fe_{2-x}Ni_x$ at 809 °C, the transition reaction L + ($Al_{13}Fe_4$) ↔ $Al_9Fe_{2-x}Ni_x$ + (Al) at 650 °C and the eutectic reaction L ↔ Al + Al_3Ni + $Al_9Fe_{2-x}Ni_x$ at 638 °C. Chumak and co-workers[23] reported that the reactions of the $Al_{10}Fe_{4-x}Ni_x$ phase formation are unknown, although Budberg *et al.*[20] with reference to Khaidar *et al.*[19] presented an invariant reaction of L + τ_2 ↔ Fe_4Al_{13} + Ni_2Al_3, whto the unit cell parameters

ich occurred in a narrow temperature range between 1050 °C and 950 °C. $Al_{10}Fe_{4\text{-}x}Ni_x$ was denoted by τ_2 in that study.

The last ternary phase of the Al-Ni-Fe system with Al ≥ 70 at. pct is a quasicrystal phase with the formula $Al_{71}Fe_5Ni_{24}$, denoted by τ_3. This phase was first discovered in 1989.[42] Later, the parameters were refined,[43,44,45] It was specified that the homogeneity range of this phase is extremely narrow, less than 1 at. pct. The compound is stable only in a slim temperature range between 847 °C and 930 °C, and the phase can be studied only after rapid quenching.

In Al-based alloys (Al ≥ 70 at. pct) with La and TM, the binary phase $Al_{11}La_3$ was discovered[46] as well as an Al_4La phase.[47] These phases were characterized by very close crystal lattice parameters and the SGs *Immm* and *Imm2* (Table I), which could not be resolved by XRD or ED. Gomes de Mesquita and Buschow[48] asserted that the low-temperature phase (α) should be described by the formula $Al_{11}La_3$, not by Al_4La. According to Buschow[49] and Gschneidner and Calderwood,[50] the

Table I. Structural Data for Al-Rich Phases (> 70 Pct) in the Al-La-Fe-Ni System

#	Phase	Space Group	Prototype	Crystal Class	Lattice Parameters (nm)	Reference
1	Al	$Fm\bar{3}m$	Cu	cubic	a = 0.405	55
2	Al_3Ni	*Pnma*	Fe_3C	orthorhombic	a = 0.661 b = 0.736 c = 0.481	27
3	Al_9Ni_2	$P2_1/c$	Al_9Co_2	monoclinic	a = 0.62 b = 0.85 β = 95 deg	28
3	Al_5 Fe_2	*Cmcm*	Unknown	orthorhombic	a = 0.767 b = 0.64 c = 0.42	30, 31
4	Al_3Fe $Al_{13}Fe_4$ $(Al_{3.2}Fe)$ $(Al_{9.75}Fe_3)$	*C2/m*	Unknown	monoclinic	a = 1.548 b = 0.808 c = 1.247 β = 107.43 deg	56 to 58
5	Al_9Fe_2	$P2_1/a$	Al_9Co_2	monoclinic	a = 0.869 b = 0.635 c = 0.632 β = 93.4 deg	33
6	Al_6Fe	$Ccm2_1$	Al_6Mn	orthorhombic	a = 0.646 b = 0.744 c = 0.877	35
7	$Al_{71}Fe_5Ni_{24}$			quasi-crystalline decagonal		43
8	Al_5FeNi $Al_{10}Fe_{4-x}Ni_x$	$P6_3/mmc$	Al_5Co_2	hexagonal	a = 0.7693 c = 0.7657	23, 36, 41
9	$Al_9Fe_{2-x}Ni_x$	$P2_1/c$	Al_9Co_2	monoclinic	a = 0.62406 b = 0.62993 c = 0.85992 β = 95.129 deg	23, 36
10	Al_3La	$P6_3/mmc$	Ni_3Sn	hexagonal	a = 0.6667 c = 0.4619	59
11	$Al_{11}La_3$	*Immm*	$Al_{11}La_3$	orthorhombic	a = 0.4431 b = 1.3142 c = 1.0132	48
12	Al_4La (β-$Al_{11}La_3$)	*I4/mmm*	Al_4Ba	tetragonal	a = 0.4422 c = 1.021	49, 60
13	Al_4La	*Imm2*	—	orthorhombic	a = 0.443 b = 1.314 c = 1.013	61
14	Al_8Fe_2La	*Pbam*	Al_8Fe_2La	orthorhombic	a = 1.257 b = 1.445 c = 0.4063	51
15	$Al_{10}Fe_2La$	*Cmcm*	$Al_{10}Fe_2Yb$	orthorhombic	a = 0.9051 b = 1.0249 c = 0.9122	62
16	$Al_{6-x}Ni_{1+x}La$	*P4/mmm*	unknown	tetragonal	a = 0.4189 c = 0 8032	63

transition of α-$Al_{11}La_3$ to the high-temperature phase β-$Al_{11}La_3$ occurs at 915 °C.

In the Al-rich corner of the Al-Fe-La system, two ternary compounds were found: Al_8Fe_2La, which was claimed to be isostructural to Al_8Fe_2Ce,[51] and $Al_{10}Fe_2La$.[52]

Thus, the results of the microstructural studies of Al-Ni-Fe-La-based alloys with Al ≥ 70 at. pct demonstrated a variety of intermetallic phases formed in different concentration ranges of the alloying elements. Moreover, minor deviations in the chemical composition led to changes in the phase composition. Therefore, the ambiguity of the results requires a careful study of the phase content in these alloys.

Previously, we performed a preliminary study of quaternary Al-La-Ni-Fe alloys and discovered the $Al_8Fe_{2-x}Ni_xLa$ phase,[53] which is isostructural to Al_8Fe_2Eu.[54] However, the atomic structures of the defects in that phase were not considered. In this paper, we present the results of a comprehensive microstructural study of the ternary and quaternary phases in air-cast $Al_{85}Ni_{11-x}Fe_xLa4$ (where x = 2 and 4 at. pct) polycrystalline alloys by means of optical microscopy (OM), scanning electron microscopy (SEM), transmission electron microscopy (TEM), scanning transmission electron microscopy (STEM), energy-dispersive X-ray (EDX) microanalysis, and X-ray diffraction (XRD). The defects in the quaternary $Al_8Fe_{2-x}Ni_xLa$ phase together with the thermal stability of the ternary and quaternary phases were studied. Based on these data, a sequence of solid-phase reactions in these alloys during cooling and heating is proposed.

II. EXPERIMENTAL PROCEDURE

Polycrystalline alloys with compositions determined as $Al_{85}Ni_7Fe_4La_4$ and $Al_{85}Ni_9Fe_2La_4$ were obtained from a melt as ingots by cooling in air. To study the thermal stability, the specimens were annealed under an Ar/H (H-4 pct) gas mixture at 400 °C, 500 °C, and 600 °C for 3 hours. The heating and cooling rates were 30 °C/min and 50 °C/min, respectively.

An Axiovert 40 MAT optical microscope was used in the first stage. The tint etching of the specimens after mechanical grinding and polishing was performed in a mixture consisting of 3 pct HF, 4 pct HNO_3, 3 pct HCl, and 90 pct H_2O at room temperature for 10 seconds. Further studies were performed by SEM/EDX microanalysis. ImageJ software (NIH) was used for the OM image processing. A focused ion beam (FIB)/SEM dual-beam Helios (FEI) at an accelerating voltage of 2 kV was used for the imaging. Due to the use of a lens detector even in secondary electron (SE) registration mode, a significant fraction of backscattering electrons (BSE) was detected that generated a strong Z-contrast. The microscope was equipped with an EDX spectrometer (EDAX), and the spectra and elemental maps were recorded using an accelerating voltage of 15 to 30 kV. The specimens for the TEM, STEM, and ED studies were prepared by 2 methods: (A) by twin-jet electropolishing in a TenuPol-5 facility (Struers) using an electrolyte consisting of 70 pct butanol, 20 pct perchloric acid, and 10 pct ethanol at a temperature of 5 to 7 °C and a potential of 40 V and by cleaning with Ar^+ ions using a PIPS (Gatan) at an acceleration voltage of 0.1 to 1 kV and (B) by using a standard lift-out FIB technique. Microstructural analyses were performed in a Titan 80 to 300 TEM/STEM (FEI) equipped with a spherical aberration corrector (probe corrector) with an accelerating voltage of 300 kV. Such a configuration allows one to obtain images in STEM mode with a resolution of 0.08 nm. The device is equipped with an EDX Si(Li) spectrometer (EDAX), a high-angle annular dark-field (HAADF) electron detector (Fischione), and a Gatan image filter (GIF) (Gatan). In addition, some of the STEM images were obtained in an aberration-corrected (probe-corrected) TITAN 80-200 (FEI) at an accelerating voltage of 200 kV. This instrument is also equipped with an HAADF detector (Fischione) and a silicon drift detector (SDD), *i.e.*, a Super-X EDX detector (Bruker). Image processing was performed using a digital micrograph (Gatan) and TIA (FEI) software. Simulations of the ED patterns and images were produced using Stadelmann's EMS software package.[64] The powder XRD analysis of the as-received and annealed bulk polycrystalline samples of the two compositions was performed with a Rigaku Miniflex-600 diffractometer (Rigaku Corporation, Tokyo, Japan). The XRD data were recorded using Cu-Kα radiation (40 kV, 15 mA, Ni-K$_\beta$ filter) in the 2θ range of 10 to 90 deg at a scan rate of 0.5 deg/min. The crystalline phases were identified with integrated X-ray powder diffraction software (PDXL: Rigaku diffraction software) and ICDD PDF-2 datasets (Release 2014 RDB). For these experiments, specimens with a size of ~ 4 × 10 mm^2 were polished on one side.

III. RESULTS

Below, in the microscopy section, we will describe in more detail the microstructure of the $Al_{85}Ni_7Fe_4La_4$ alloy because the phase content and overall microstructure in the two alloys are similar. The XRD data and the results of the annealing are presented for both alloys.

A. *OM Microstructure Study*

The OM image after the tint etching of the $Al_{85}Ni_7Fe_4La_4$ alloy is shown in Figure 1. An analysis of the contrast and morphology of the particles allows us to conclude that at least 4 phases are present in the alloy. Typical images of the particles of each phase are indicated by numbers from "1" to "4." A further study has shown that the particles marked by "1" with light contrast are fcc-Al. These particles look polycrystalline in nature and reach up to 50 μm in size. The second type of particles denoted by "2" looks bluish in OM, and they have been identified as $Al_9Ni_{2-x}Fe_x$. These particles often adopt an elongated morphology with a length of up to 20 μm and width of 1 μm. They are observed in two media: 1—surrounded by the fcc-Al matrix and 2—around relatively large elongated particles of the $Al_8Fe_{2-x}Ni_xLa$ phase designated by "4." These four component particles are polycrystalline agglomerates with a grain size of 5 to 20 μm and a total size of 100 μm; they have a brown tint in OM images, which is apparently due to the presence of Fe. The facetted particles in gray color with sizes up to 25 microns are

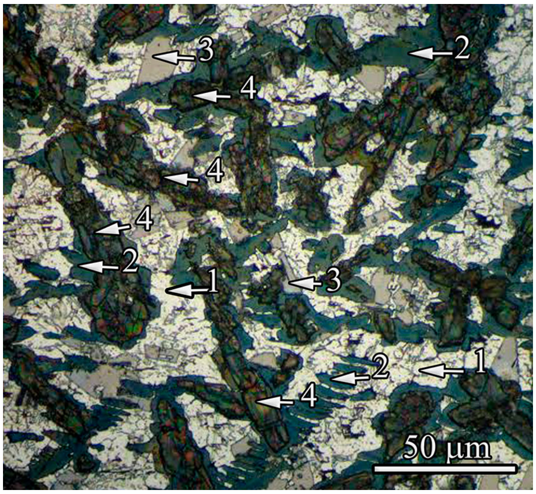

Fig. 1—Typical microstructure of the $Al_{85}Ni_7Fe_4La_4$ alloy (OM image). Phases are denoted by 1—Al, 2—$Al_9Ni_{1-x}Fe_x$, 3—$Al_{11}La_3$, and 4—$Al_8Fe_{2-x}Ni_xLa$.

identified as the $Al_{11}La_3$ phase, which is indicated by "3" in Figure 1. According to a previous paper,[48] we designated that phase by "11-3", not by "4-1," which reflects the stoichiometric Al/La atomic ratio. While evaluating the OM images of different phases, we estimated their volume fraction in the $Al_{85}Ni_7Fe_4La_4$ and $Al_{85}Ni_9Fe_2La_4$ alloys. Relatively small differences in the Fe and Ni contents in the alloys resulted in an approximately twofold increase of the $Al_9Ni_{2-x}Fe_x$ phase in the Ni-rich $Al_{85}Ni_9Fe_2La_4$ alloy. In contrast, the content of the $Al_8Fe_{2-x}Ni_xLa$ phase is twice as high as that in the $Al_{85}Ni_7Fe_4La_4$ alloy.

B. *SEM and EDX Microanalysis*

Representative SEM images obtained from the $Al_{85}Ni_7Fe_4La_4$ alloy are presented in Figures 2(a) and (b). Due to the essential Z-contrast, the Al particles denoted by "1" look darkest. However, in the high-magnification images, the contrast is uneven in these areas, possibly due to the polycrystalline microstructure, intermetallic precipitates, and defect formation during the crystallization or specimen preparation.

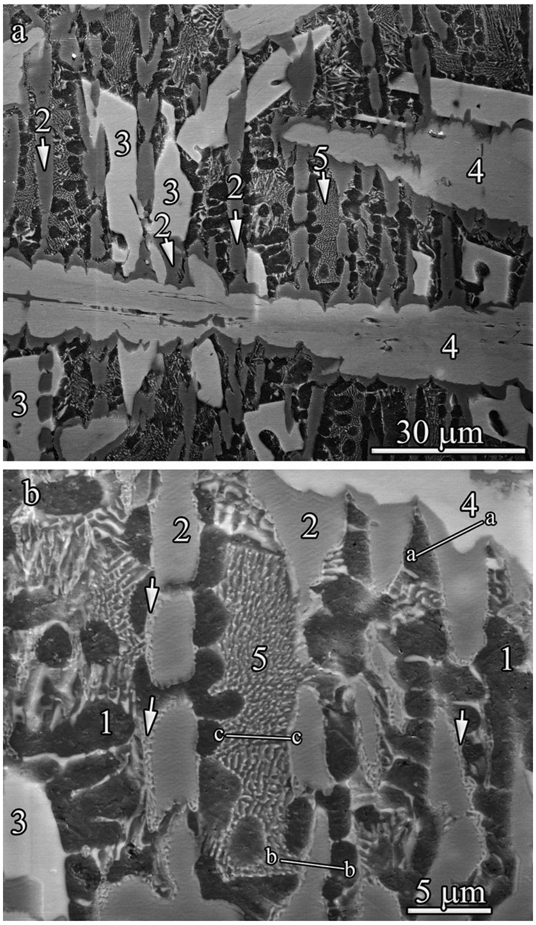

Fig. 2—SEM image of the $Al_{85}Ni_7Fe_4La_4$ alloy showing the microstructure at (*a*) low and (*b*) high magnifications. Phases are denoted by 1—Al, 2—$Al_9Ni_{1-x}Fe_x$, 3—$Al_{11}La_3$, 4—$Al_8Fe_{2-x}Ni_xLa$, and 5—Al-Al_{11} La_3-$Al_3Ni_{1-x}Fe_x$ eutectic. The "a-a", "b-b" and "c-c" sections indicate the areas where lamellas were cut. The arrows in (b) show the eutectic microstructure.

The particles $Al_8Fe_{2-x}Ni_xLa$ denoted by "4" in Figures 2(a) and (b) exhibit bright contrast due to the presence of La. It is sometimes difficult to distinguish between these and $Al_{11}La_3$, denoted by "3" on the SEM images, but the presence of TM can be unambiguously detected using EDX microanalysis elemental mapping, and these maps are shown in Figures 3(a) through (f).

Number "2" denotes the $Al_9Ni_{2-x}Fe_x$ particles. These particles look brighter than the Al particles, and they adopted an elongated morphology with a 2.5:1 mean aspect ratio. As is clearly visible in Figures 2(a) and (b), the $Al_9Ni_{2-x}Fe_x$ particles are oriented in one direction. The particles with the same contrast surround the $Al_8Fe_{2-x}Ni_xLa$ quaternary phase particles forming the core shell, which is also visible in the multiple element map (Figure 2(f)). This microstructure is typical for the initial stage of the peritectic transformation in the alloy that was quenched to room temperature, as is described in a book[65] and the corresponding references. The $Al_9Ni_{2-x}Fe_x$ particles together with $Al_8Fe_{2-x}Ni_xLa$ form a two-axis dendritic microstructure. Such a dendritic microstructure could be formed at the initial stages of crystallization from the melt. Adjacent to the $Al_9Ni_{2-x}Fe_x$ particles, eutectic structures with well-defined dispersed $Al_{11}La_3$ particles are shown by arrows in Figure 2(b). In addition, larger similar eutectic areas were found; they are denoted by "5" in Figures 2(a) and (b). In some areas, a coarser eutectic structure was found. A more detailed study of the eutectic structures was carried out by TEM, STEM, and EDX microanalysis, and the results are presented below.

C. *TEM, STEM, ED and EDX Microanalysis Study*

An HAADF STEM image of the specimen prepared by FIB from the section denoted by "a-a" in Figure 2(b) is presented in Figure 4(a). The contrast variations together with the EDX spectroscopy (EDXS) data (Figure 4(b)) unambiguously indicated that there are four phases in the cut lamella, namely, fcc-Al, $Al_{11}La_3$, $Al_9Ni_{2-x}Fe_x$, and $Al_8Fe_{2-x}Ni_xLa$. The results of the EDXS study are presented in Table II. Below, the crystal structures and chemical compositions of all the phases starting from quaternary and moving to binary phases are considered in detail. The HAADF STEM image demonstrated more clearly than the SEM images that there is a layer consisting of $Al_9Ni_{2-x}Fe_x$ particles surrounding the $Al_8Fe_{2-x}Ni_xLa$ particles, as shown in the frame in Figure 4(a). An analysis of the BF TEM image of the same area presented in Figure 4(b) revealed the polycrystalline nature of the $Al_8Fe_{2-x}Ni_xLa$ cluster and the $Al_9Ni_{2-x}Fe_x$ layer. The $Al_8Fe_{2-x}Ni_xLa$ particles exhibit an irregular morphology and grain sizes ranging between 0.2 and 1 μm. Many of these particles show contrast characteristics of planar defects, which are denoted by arrows in Figure 4(b). The defect density was estimated from this image and similar images and was up to 10^9 cm^{-2}. The crystal structures of these defects can be determined by the HAADF STEM technique, and the details are presented below.

A preliminary study of the quaternary $Al_8Fe_{2-x}Ni_xLa$ phase indicated that it exhibited an orthorhombic

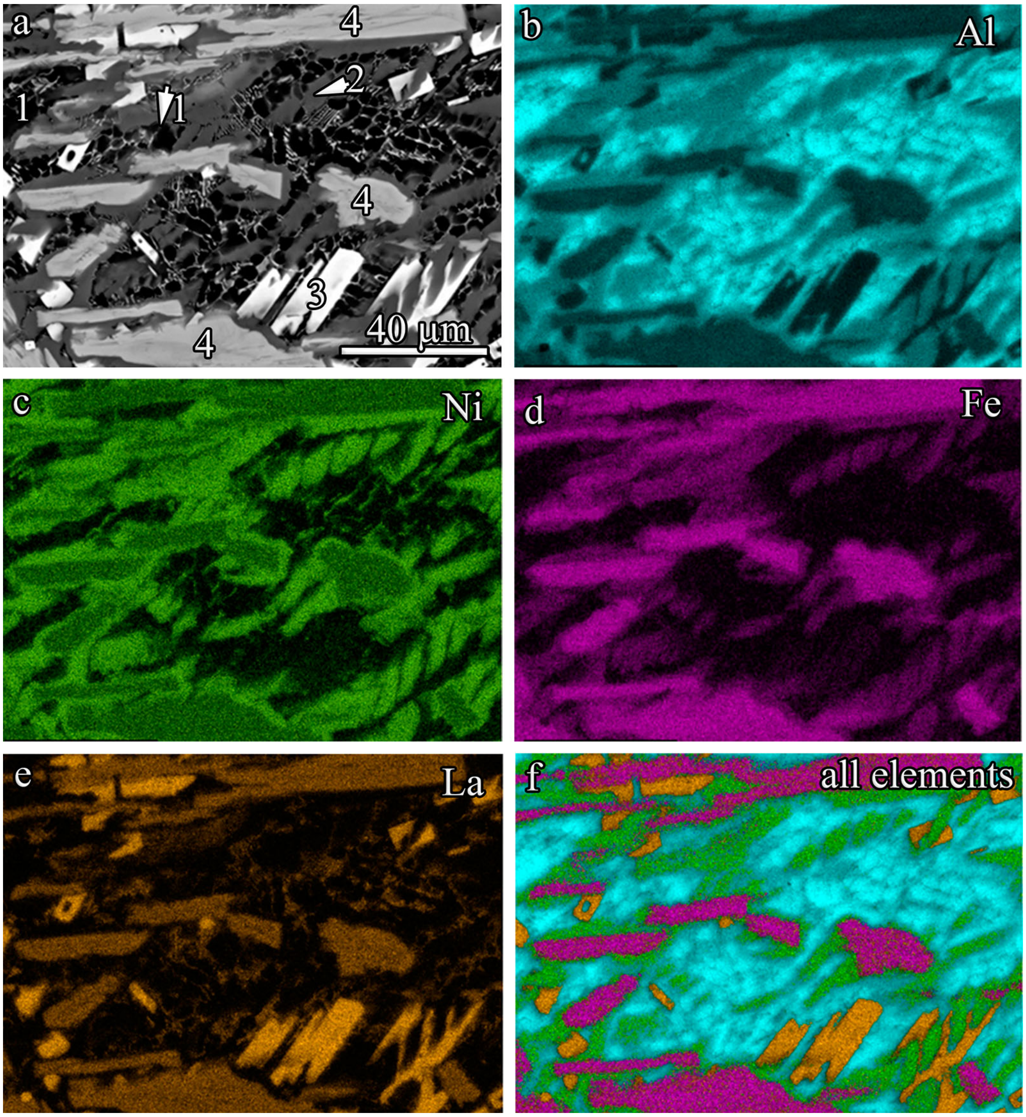

Fig. 3—(*a*) SE SEM image of the $Al_{85}Ni_7Fe_4La_4$ alloy (phases are denoted by 1—Al, 2—$Al_9Ni_{1-x}Fe_x$, 3—$Al_{11}La_3$, 4—$Al_8Fe_{2-x}Ni_xLa$) and corresponding EDX elemental maps for (*b*) Al, (*c*) Ni, (*d*) Fe, (*e*) La, and (*f*) all elements.

crystal structure isostructural to Al_8Fe_2Eu (SG *Pbam*).[53] The high-resolution (HR) HAADF STEM image of that phase obtained in the [001] zone axis is presented in Figure 5(a). The most intense spots on the image correspond to the La atom column, and the Ni and Fe atom columns give rise to spots with a nearly equal intensity, which can prove a substitution of Ni and Fe atoms. The weakest contrast comes from the column of Al atoms. The selected area electron diffraction (SAED) pattern from an $Al_8Fe_{2-x}Ni_xLa$ particle in the [001] zone axis is presented in Figure 5(b). One of the peculiarities of the SAED is the streaks in the direction parallel to $\boldsymbol{0k0}^*$ that arise from the defects with the habit plane parallel to {0k0}. The $Al_8Fe_{2-x}Ni_xLa$ 4x4 unit cells in the [001] projection are shown in Figure 5(c); one of the unit cells is highlighted by a yellow rectangle. There are structural elements shown by red rectangles with La atoms in the corners and the sides, parallel to {310} and {140}. These rectangles are shifted relative to each other at a distance equal to the *a* and *b* parameters of the unit cell, and their mutual position is very helpful in understanding the crystal structure of the defects in the $Al_8Fe_{2-x}Ni_xLa$ phase.

A close inspection of the HR HAADF STEM image presented in Figure 5(a) and similar images obtained in the same projection revealed a variety of flat defects, denoted by “1” to “4”, and dislocation cores associated with flat defects, denoted by “5”. The flat defects denoted by “1” in Figure 5(a) are mostly distinctive, and these defects are marked by arrows in Figure 4(b). An enlarged HAADF STEM image of that defect is presented in Figure 6(a). An analysis of these defects with the habit plane parallel to the ***a***-axis of the $Al_8Fe_{2-x}Ni_xLa$ crystal reveals that these defects are δ-layers of the monoclinic $Al_{3.2}Fe_{1-x}Ni_x$ phase with the $Al_{3.2}Fe$ structure type (SG *C2/m*).[56] Each δ-layer consists of adjacent staggered pentagons with Fe(Ni) atom columns located in the corners, and in the center,

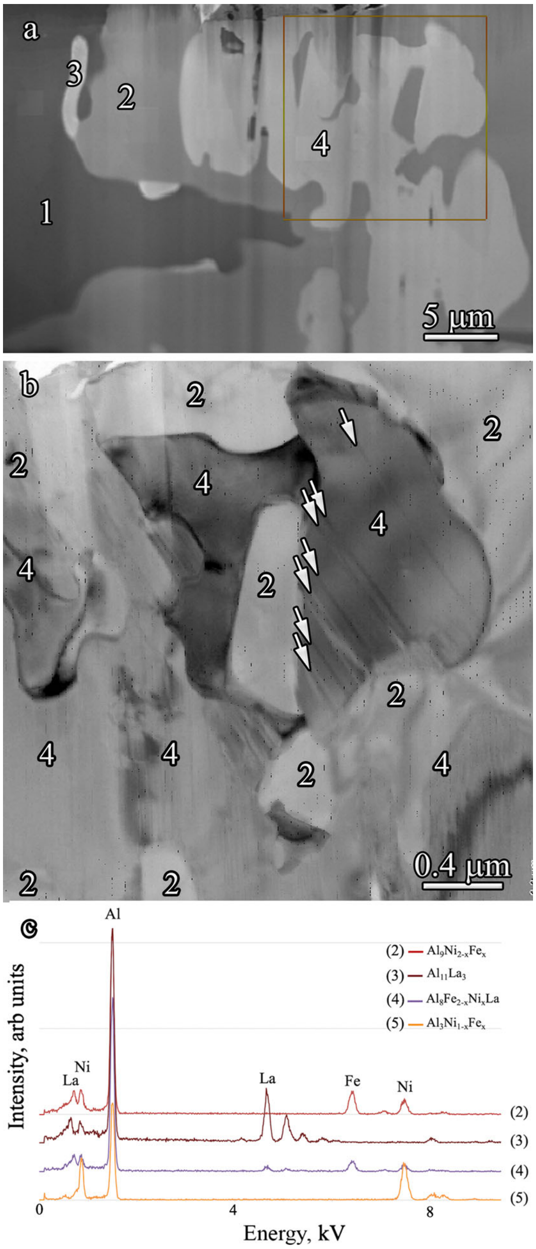

Fig. 4—(*a*) HAADF STEM image of the specimen prepared by FIB in the area of the "a-a" section (see Fig. 2(b)): phases are denoted by 1—Al, 2—$Al_9Ni_{2-x}Fe_x$, 3—$Al_{11}La_3$, and 4—$Al_8Fe_{2-x}Ni_xLa$. (*b*) Enlarged BF TEM image of the part of the specimen shown by the red rectangle in (a). Phases are denoted by 2—$Al_9Ni_{1-x}Fe_x$ and 4—$Al_8Fe_{2-x}Ni_xLa$. Flat defects in the $Al_8Fe_{2-x}Ni_xLa$ particle are indicated by arrows. (*c*) Typical EDX spectra from $Al_9Ni_{2-x}Fe_x$, $Al_{11}La_3$, $Al_8Fe_{2-x}Ni_xLa$ and $Al_3Ni_{1-x}Fe_x$ particles.

the pentagons adopted a mirror (*m)* symmetry position. The pentagons are highlighted in red Figures 6(a) and (b). These defects were described in Reference 53; however, their composition, and the presence of Ni in particular, was not determined. The EDX elemental mapping (Figures 6(c) through (f)) unambiguously reveals the presence of Ni at the Fe sites in these δ-layers without any ordering. A light blur of the image in the δ-layer area could be linked with Al atomic substitution for Ni and Fe. Thus, the chemical content

Table II. Results of the EDXS Study of the Areas Denoted by "1" Through "4" in Fig. 4(a)

		Element Content, At. Pct			
	Phase	Al	Ni	Fe	La
1	Al	99	1	0	0
2	$Al_9Ni_{2-x}Fe_x$	82	15	3	—
3	$Al_{11}La_3$	80	—	—	20
4	$Al_8Fe_{2-x}Ni_xLa$,	71	9	11	9

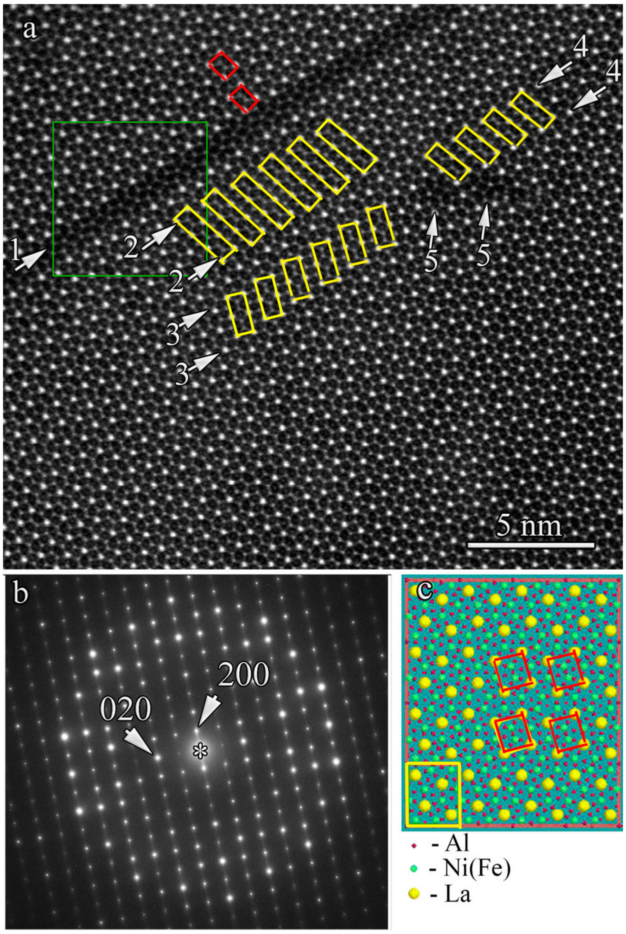

Fig. 5—(*a*) HR HAADF STEM image of an $Al_8Fe_{2-x}Ni_xLa$ particle obtained in the [001] zone axis. The areas with flat defects are between the arrows with numbers "1-4." The structural elements are shown by red rectangles with La atoms in the corners and the sides, parallel to {310} and {140}, and the defects that can be explained using these structural elements are shown by the yellow rectangle. The dislocation cores are denoted by "5". (*b*) SAED from an $Al_8Fe_{2-x}Ni_xLa$ particle in the [001] zone axis. (*c*) $Al_8Fe_{2-x}Ni_xLa$ 4 × 4 unit cells in the [001] projection (Color figure online).

of the phase in the δ-layers can be described as $Al_{3.2}Fe_{1-x}Ni_x$.

The abovementioned structural elements, which are highlighted by red rectangles with columns of La atoms in the corners shown in Figures 5(a) and (c), are used for the description of the planar defects. The stacking fault (SF) forms a triple chain of these structural elements,

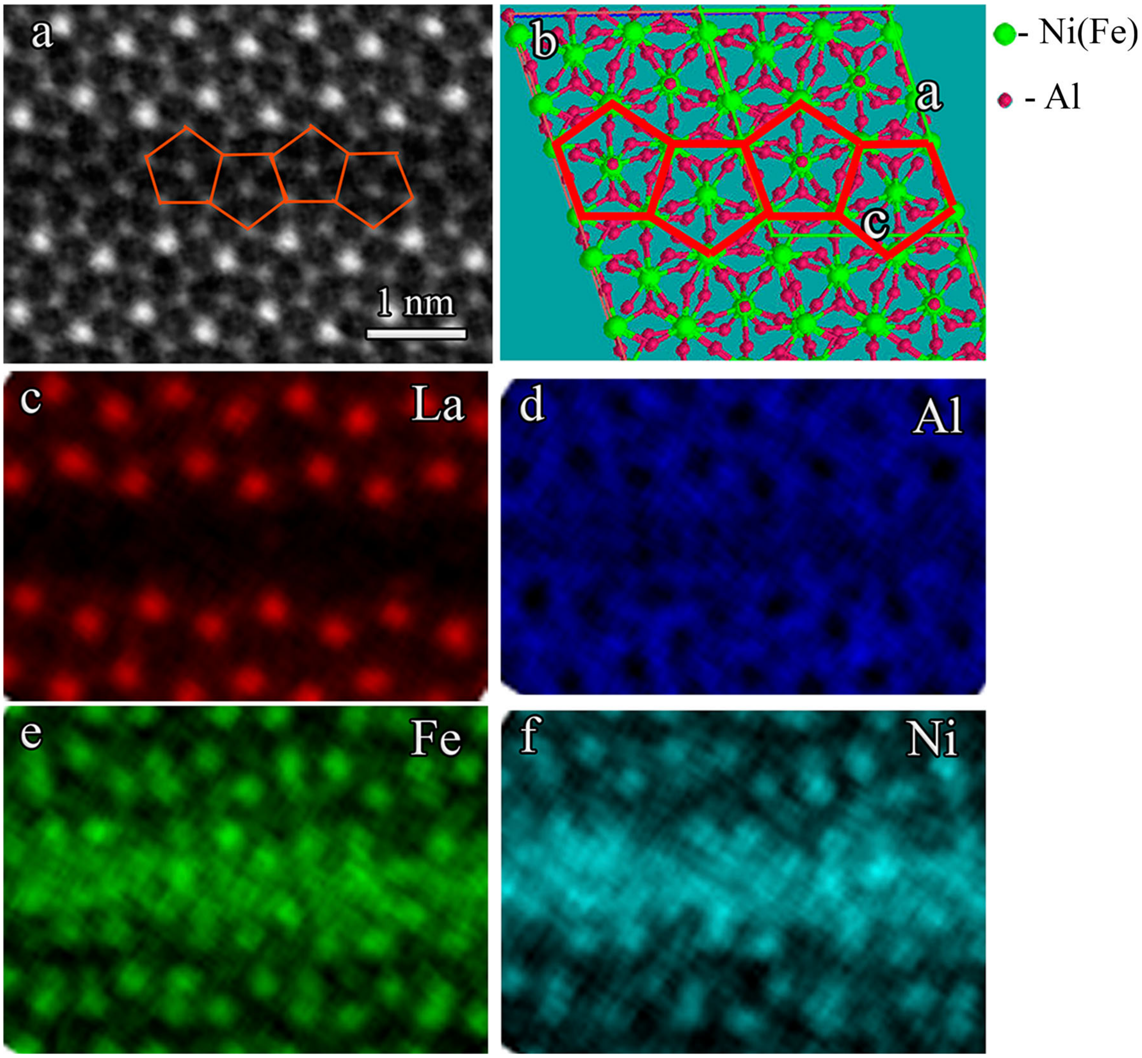

Fig. 6—(*a*) HAADF STEM image of planar defect "1," which consists of δ-layers of the monoclinic $Al_{3.2}Fe_{1-x}Ni_x$ phase. (*b*) Model of the defect and EDX elemental maps for (*c*) La, (*d*) Al, (*e*) Fe, and (*f*) Ni.

and that SF is confined within the arrows marked by "2." The model of that defect, which is below denoted by the second type, is presented in Figure 7(a); its formation was caused by the $a/2$ (half unit cell) shift of the adjacent areas. This defect may be defined as out-of-phase boundaries; however, out-of-phase boundaries are typically associated with layered compounds,[66,67] Although the $Al_8Fe_{2-x}Ni_xLa$ crystal structure does not represent a layered structure, we still believe that we can use that definition in our case.

Defects of the third type are also shown by arrows marked by "3" and "4" in Figure 5(a). Such a defect can be described as shifted mirror twins. The defect models are presented in Figures 7(b) and (c), respectively. These defects are located between the arrows marked by "3" and "4" and are formed by the twin formation with a simultaneous shift by $3a/4$ along the ***a***-axis, resulting in the formation of double chains of the structural units. The defects that are located between the arrows marked by "3" and "4" in Figure 5(a) are symmetrical relative to the mirror plane parallel to the ***b*** axis but with a $b/2$ shift along the ***b*** axis. In the junction area of these two defects, dislocations are formed without La in the dislocation cores, as observed in the HR HAADF STEM images and supported by EDXS elemental mapping (not presented here).

Two closely spaced dislocation cores are indicated by "5" in Figure 5(a). The dislocations were formed as a result of the interaction of two flat defects, namely, "3" and "4." It was difficult to construct the Burgers circuit around the dislocation cores; however, the observation of the micrograph at a glancing angle parallel to the ***a***-axis of the $Al_8Fe_{2-x}Ni_xLa$ unit cell does not reveal any extra planes. Thus, we proposed that the Burgers vector of the dislocations is parallel to the ***a***-axis. Surprisingly, the HR HAADF STEM image unambiguously demonstrated the absence of rare-earth La atoms in the dislocation core areas. The cores of the screw dislocations in $SrTiO_3$, in contrast, demonstrated vacancies in the Ti-O column, not the Sr ones.[68]

An HR HAADF STEM image of another defect in the $Al_8Fe_{2-x}Ni_xLa$ compound together with the EDXS

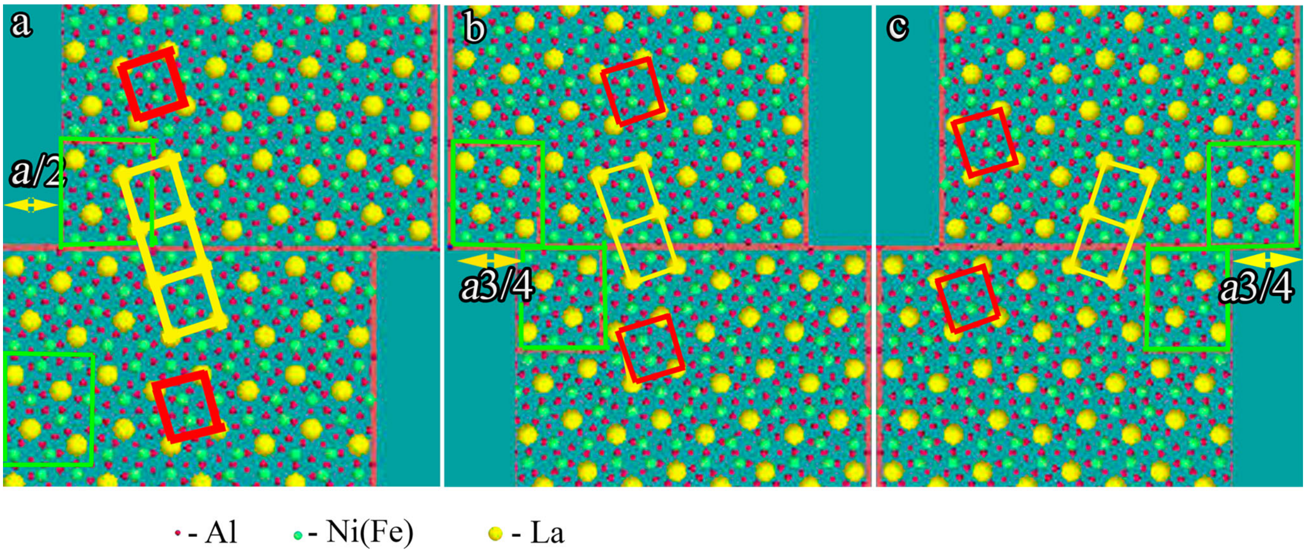

Fig. 7—Models of the defects marked by arrows in Fig. 5(a). (*a*) "2" is the out-of-phase boundary. (*b*) and (*c*) are "3" and "4," the mirror twins with shifts in opposite directions.

elemental maps is presented in Figures 8(a) through (e); the model is shown in Figure 8(f). La, Ni, Fe and Al atoms are present in the defect area. This defect has a typical zig-zag contrast; the habit plane parallel to $\{140\}$ occurs due to the overlap of the defect of the third type with the matrix. In Figures 8(a) and (f), one can see two adjacent structural elements from the defected part of the specimen marked with pairs of yellow rectangles and the third one belonging to the matrix, which is single and shifted relative to the double structural element. It should be noted that the intensity of the spots corresponding to the La columns in the zig-zag defect area is lighter than that in the other parts of the specimen due to a reduced number of atoms in the La columns in the zig-zag defect area relative to other areas since the defect area is an overlapping of two crystals. The same reduction of the spot intensity is visible in the La elemental map.

The composition of the quaternary phase was measured using EDXS, and consistent results were obtained from several particles. The quantification error within the obtained spectra was ~ 5 pct. However, the quantification of the spectra was complicated due to the lack of a suitable quaternary standard, the relatively large uncertainty in the compositions of the ternary and binary phases containing Fe and Ni, which can substitute for each other, and the high defect density in the particles. The composition of the quaternary phase is Al:Fe:Ni:La = 8:1.1:0.9:1. A typical EDXS spectrum is presented in Figure 4(c). Therefore, the quaternary phase can be described by the general formula $Al_8Fe_{1.1}Ni_{0.9}La$, which is consistent with the stoichiometry Al:TM: La = 8:2:1.

For the TEM and EDXS investigations of the ternary Al-Ni-Fe compound, several lamellas in the sections marked by "a-a", "b-b", and "c-c" in Figure 2(b) were prepared from the sample. First, the "a-a" lamella was sectioned in the area of the $Al_9Ni_{2-x}Fe_x$ particle adjacent to the $Al_8Fe_{2-x}Ni_xLa$ particle, and the images are presented in Figures 4(a) and (b). The SAED pattern obtained from the $Al_9Ni_{2-x}Fe_x$ particle is presented in Figure 9(a). The analysis of the SAED unambiguously confirmed that the crystal structure of that particle adopted a monoclinic Al_9Co_2-type structure with SG $P2_1/c$. That phase was discovered in a number of studies considered above in the introduction. The SAED pattern presented in Figure 9(a) corresponds to the [011] zone axis, and the 100 reflections arise from double diffraction. To estimate the lattice parameters of the $Al_9Ni_{2-x}Fe_x$ phase, we verified the camera length calibration using adjacent Al particles and found a = 0.857 nm, b = 0.629 nm, c = 0.621 nm, and β = 97 deg, close to the unit cell parameters of Al_9Co_2[69]). The EDXS quantification indicated that the Fe content in the $Al_9Ni_{2-x}Fe_x$ particle in our alloys, namely, Ni = 15 ± 1 at. pct, Fe = 3 ± 1 at. pct, was lower than that in the studies of Khaidar *et al.*[19] and Chumak *et al.*[23] but corresponded to the homogeneity region determined in the studies of Dybkov *et al.*[29] and Eleno *et al.*[22] The EDXS spectrum is presented in Figure 4(c), and the quantitative data are shown in Table II. Thus, the $Al_9Ni_{2-x}Fe_x$ phase can be described as $Al_9Ni_{1.6}Fe_{0.4}$.

The lamella was prepared from elongated $Al_9Ni_{2-x}Fe_x$ particles away from quaternary intermetallic particles, such as "b-b" sections, as shown in Figure 2(a). The SAED and EDXS investigations demonstrated that the crystal structure also adopted the Al_9CO_2 crystal lattice type, and its chemical composition was the same as described above.

Occasionally, smaller Al-Ni-Fe particles with different chemical contents were found. They have irregular morphologies with sizes not exceeding 1 μm. The crystal structure is typical for orthorhombic Al_3Ni compounds with the SG *Pnma*.[27] The SAED pattern obtained in the [010] zone axis is presented in Figure 9(b), and the corresponding EDXS spectra are shown in Figure 4(c).

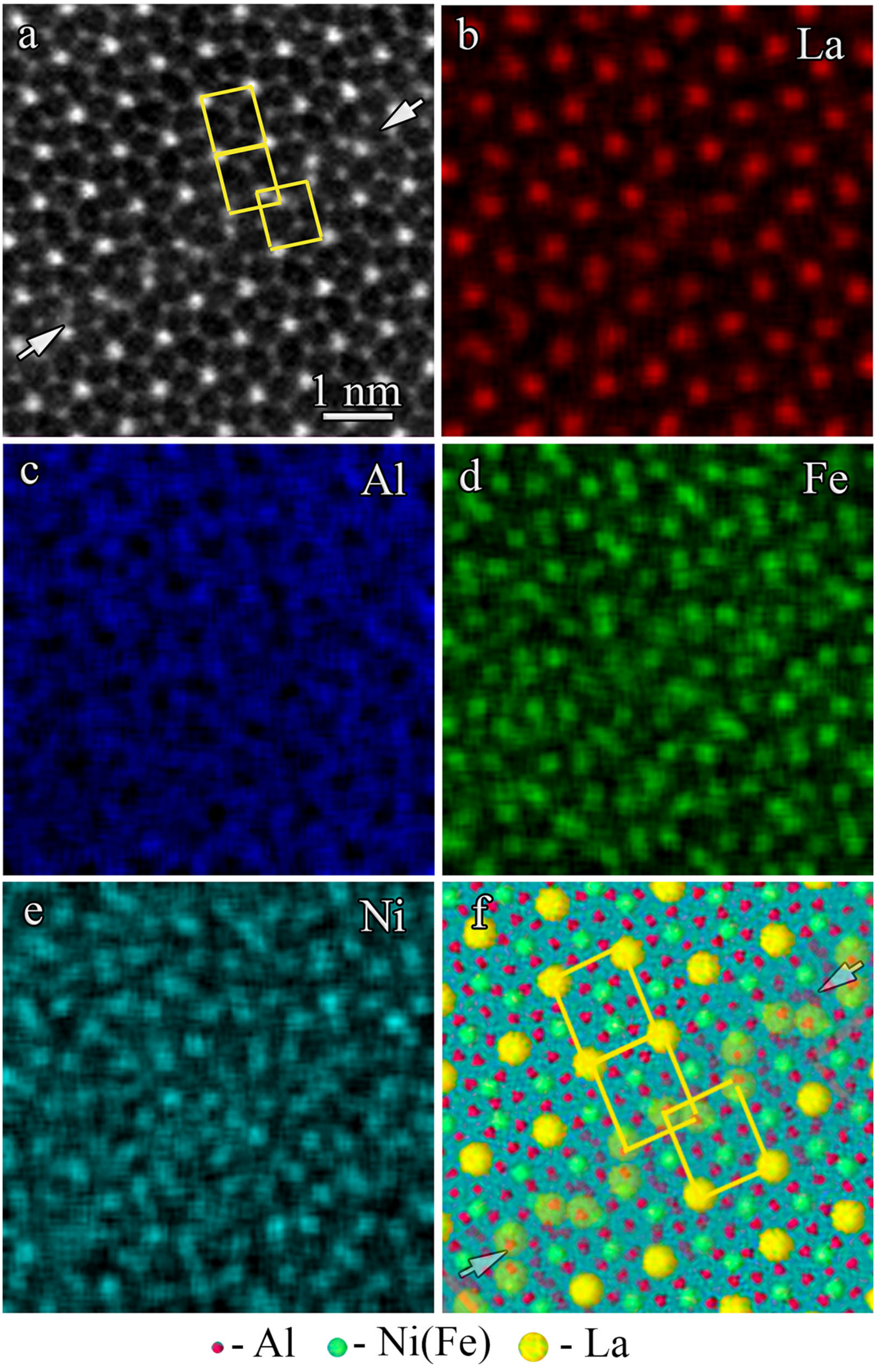

Fig. 8—(*a*) HR HAADF STEM image of the shifted mirror twin overlapping with the $Al_8Fe_{2-x}Ni_xLa$ matrix and EDX elemental maps: (*b*) La, (*c*) Al, (*d*) Fe, and (*e*) Ni. (*f*) Model of the defect.

The EDX quantification indicated a very low Fe content in the particles: Al = 75 ± 1.0 at. pct, Ni = 23.5 ± 1.0 at. pct and Fe = 1.5 ± 1.0 at. pct. The general formula for these particles might be $Al_3Ni_{1-x}Fe_x$, where $x = 1.5$. It should be noted that the Al:TM stoichiometry is close to 3:1.

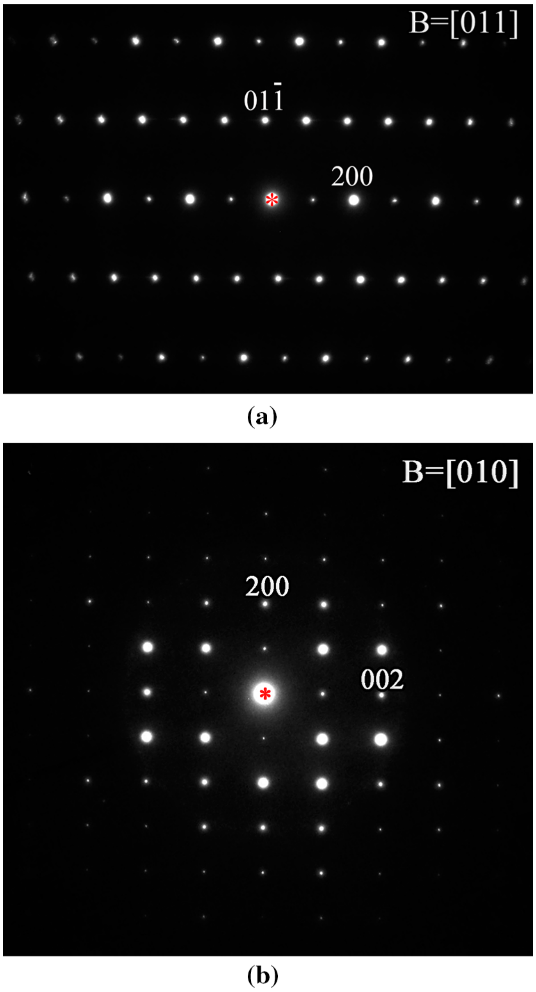

(a)

(b)

Fig. 9—(*a*) SAED obtained from an $Al_9Ni_{2-x}Fe_x$ particle in the [011] zone axis. (*b*) SAED obtained from an $Al_3Ni_{1-x}Fe_x$ particle in the [010] zone axis.

A relatively high density of these particles was found during the study of the specimens obtained from the eutectic areas, such as the "c-c" section in Figure 2(b). An HAADF STEM image of that sample together with the EDXS elemental mapping is presented in Figures 12(a) through (e). A part of a quaternary phase particle surrounded by an $Al_9Ni_{2-x}Fe_x$ shell is visible on the right side of the micrograph. The adjacent eutectic area contains fcc-Al, $Al_{11}La_3$ and $Al_3Ni_{1-x}Fe_x$ particles. The content can be confirmed by the EDXS elemental mapping, and the crystal structure was unambiguously determined by an ED study (the results are not presented here) as an orthorhombic Al_3Ni structure type with the SG *Pnma*.

The $Al_{11}La_3$ particles exhibited two types of morphology. The first type is larger faceted particles with sizes up to 20 μm, as shown by the SEM study presented in Figure 2(a), and the second is observed in the eutectic areas shown in Figure 10(a).

The ED study pointed to an orthorhombic crystal structure of the $Al_{11}La_3$ particle of both morphology types and the SG Immm or Imm2. The EDXS data (Figure 4(c)) demonstrated that the Al:La stoichiometry was close to 4:1, which could indicate that those particles corresponded to the Al_4La phase. However, taking into account the study of Gomes de Mesquta and Buschow,[48] we can suggest that the particles are $Al_{11}La_3$. A light excess Al content might arise from Al matrix fluorescence. It is worth noting that we did not observe Ni and Fe peaks in the EDXS spectra (Figure 13), in contrast to the data presented by Huang *et al.*[46]

D. *XRD Analysis*

The XRD spectra obtained from the alloys $Al_{85}Ni_7Fe_4La_4$ (***I***) and $Al_{85}Ni_9Fe_2La_4$ (***II***) are presented in Figure 11.

There are many overlapping peaks in the measured patterns that point to a multicomponent phase mixture. The most intense peaks represent fcc-Al, $Al_{11}La_3$, $Al_9Ni_{2-x}Fe_x$, and $Al_3Ni_{1-x}Fe_x$. However, the relative intensities disagree because of poor statistics, unequal particle sizes and preferred orientation effects in the measured data. The XRD spectra containing well-defined peaks that did not match those four phases could be attributed to $Al_8Fe_{2-x}Ni_xLa$. The most intense peaks, which are typical for the $Al_8Fe_{2-x}Ni_xLa$ phase, isostructural to Al_8EuFe_2,[54] are identified in both XRD spectra at angles of $2\theta = 28.20$ deg ($d = 0.316$ nm), $2\theta = 31.40$ deg ($d = 0.29$ nm), $2\theta = 34.06$ deg ($d = 0.26$ nm), and $2\theta = 36.10$ deg ($d = 0.25$ nm). The peak at the angle of $2\theta = 20.11$ deg ($d = 0.44$ nm) is definitely indexed to the (110) reflection of the monoclinic $Al_9Ni_{2-x}Fe_x$ phase. The peaks arising from $Al_{3.2}Fe_{1-x}Ni_x$ overlapped with the peaks from the other phases, which caused uncertainty in the phase identification. The noticeable broadening of the peak in the $2\theta = 43$ to 45 deg range in alloy (***I***) could suggest the presence of an $Al_{3.2}Fe_{1-x}Ni_x$ phase, since the most intense peaks of that phase are observed in that range. According to the OM study, the volume fraction of the $Al_8Fe_{2\text{-}x}Ni_xLa$ phase is higher in the Fe-rich alloy (***I***) relative to alloy (***II***); therefore, we did not observe any obvious trace of the $Al_{3.2}Fe_{1\text{-}x}Ni_x$ phase in alloy (***II***).

E. *Phase Stability and Phase Transformations*

The phase transformation temperature and phase stability were studied after isothermal annealing in vacuum at 400 °C, 500 °C, and 600 °C for 3 hours. A comprehensive microstructural study including SEM, TEM/STEM, EDS, and XRD was performed. We also used part of the data from differential scanning calorimetry (DSC) obtained in the study of Bakhteeva *et al.*[70] The DSC scan during heating and cooling was performed at a rate of 20 °C/min.

Typical SEM images of the Fe-rich $Al_{85}Ni_9Fe_2La_4$ alloy (***I***) after annealing at 400 °C, 500 °C, and 600 °C and alloy (***II***) ($Al_{85}Ni_9Fe_2La_4$) after annealing at 600 °C are presented in Figures 12(a) through (d). Coarse particles of different phases can be found in the sample after annealing at 400 °C (Figure 12(a)). However, the eutectic denoted by "5" in Figures 2(a) and (b) decomposes. At the same time, the eutectic reaction starts at

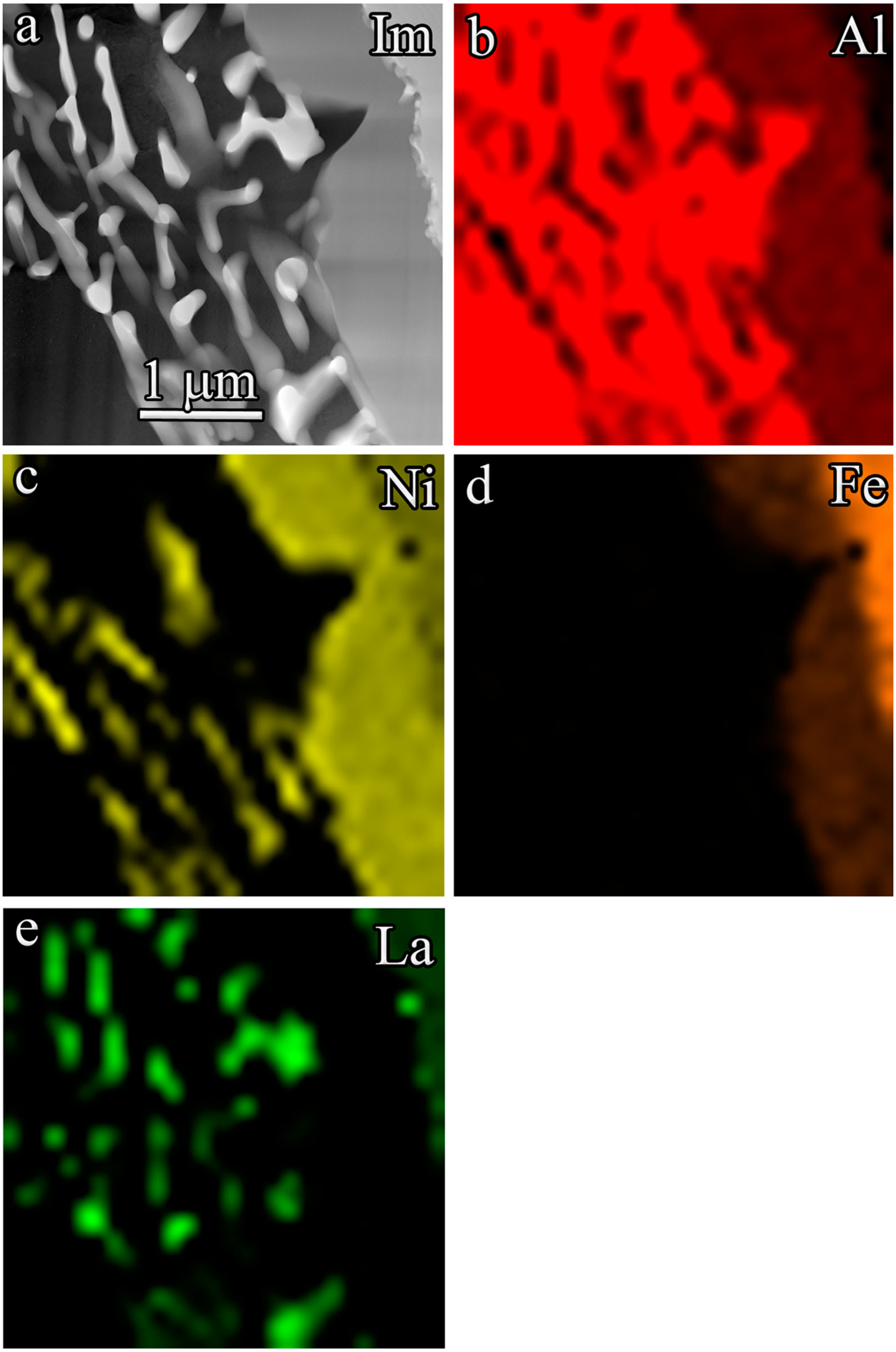

Fig. 10—Microstructure of the specimen in the "c-c" area. (*a*) HAADF STEM image of that specimen and the EDX elemental maps: (*b*) Al, (*c*) Ni, (*d*) Fe, (*e*) La.

the quaternary $\mathrm{Al_8Fe_{2-x}Ni_xLa}$ phase particles, as shown in the inset of Figure 12(a). The aspect ratio of the $\mathrm{Al_9Fe_{2-x}Ni_x}$ particles decreases. Annealing at 500 °C resulted in the eutectoid reaction

$$\mathrm{Al_{8L}aFe_{2-x}Ni_x} \rightarrow \mathrm{Al_{11}La_3} + \mathrm{Al_9Ni_{2-x}Fe_x},$$

as shown in Figure 12(b). Only coarse particles of the three phases, namely, Al, $\mathrm{Al_{11}La_3}$, and $\mathrm{Al_9Ni_{2-x}Fe_x}$, are

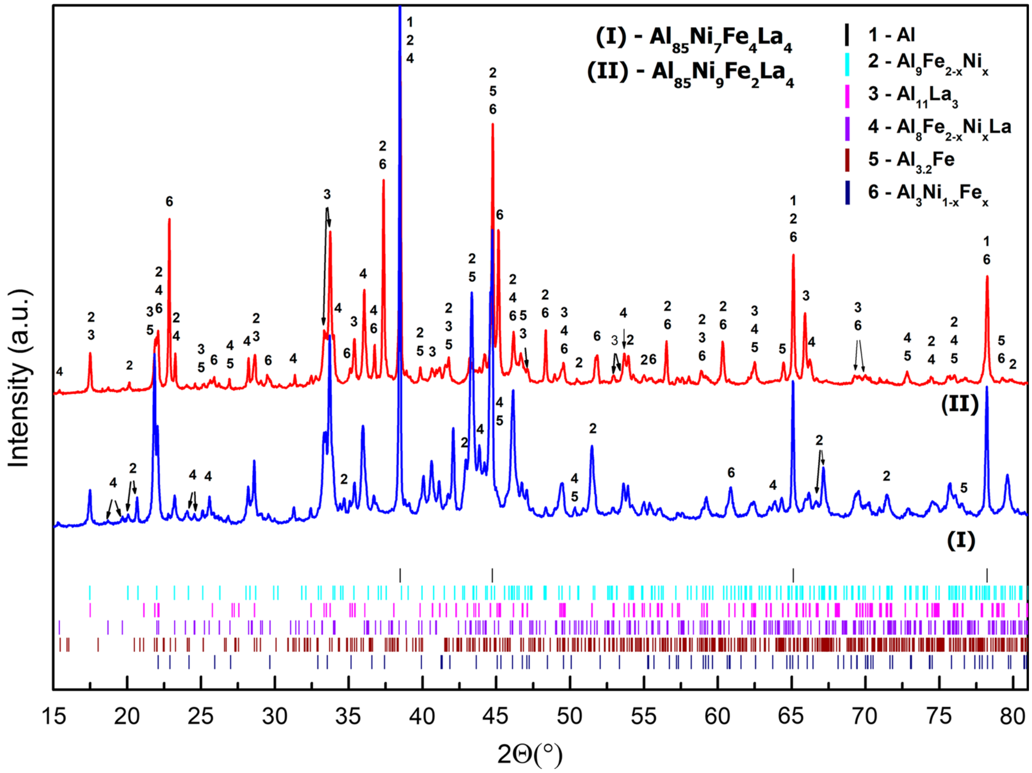

Fig. 11—XRD patterns of $Al_{85}Ni_7Fe_4La_4$ (***I***) and $Al_{85}Ni_9Fe_2La_4$ (***II***) alloys.

visible in the SEM images. After annealing at 600 °C, the coarsening of eutectics occurs, and only relatively large particles of these three phases are visible in Figure 12(c). The peculiarities of the contrast and EDXS data indicated that the $Al_3Ni_{1-x}Fe_x$ particles were formed in the $Al_{85}Ni_9Fe_2La_4$ alloy (***II***). These particles look slightly brighter than the $Al_9Fe_{2-x}Ni_x$ particles in Figure 12(d). The volume fraction of each phase after annealing at 500 °C and 600 °C was estimated using the difference in contrast between the SEM images; the results are presented in Table III.

The XRD spectra obtained from the $Al_{85}Ni_7Fe_4La_4$ (***I***) alloys after annealing at 400 °C, 500 °C, 600 °C and $Al_{85}Ni_9Fe_2La_4$ (***II***) after annealing at 600 °C are presented in Figure 13.

The peaks in the spectrum obtained from the $Al_{85}Ni_7Fe_4La_4$ (***I***) alloy after annealing at 400 °C, located in the range of $2\theta = 33$ to 34 deg on the right and left from the peaks identified as coming from the $Al_{11}La_3$ phase (denoted by "3"), are clearly visible; these peaks correspond to the $Al_8LaFe_{2-x}Ni_xLa$ phase ("4"). After annealing at 600 °C, these peaks vanish. The intensity of the peak at $2\theta = 36.10$ deg ($d = 0.249$ nm) decreases considerably, mostly due to the impact of the $Al_8Fe_{2-x}Ni_xLa$ phase ("4"). The peak at $2\theta = 36.7$ deg($d = 0.244$ nm) associated with the $Al_8Fe_{2-x}Ni_xLa$ ("4") and $Al_3Ni_{1-x}Fe_x$ ("6") phases disappeared after annealing at 500 °C or higher temperatures. Along with that, the intensity of the peaks associated with the $Al_9Ni_{2\text{-}x}Fe_x$ phase ("2") at $2\theta = 37.4$ deg ($d = 0.240$ nm) and $2\theta = 40.0$ deg ($d = 0.225$ nm) substantially increases. The intensity of the peak at $2\theta = 42.15$ deg ($d = 0.214$ nm) coming from the $Al_9Ni_{2-x}Fe_x$ phase ("2") increases after annealing up to 500 °C but then unexpectedly decreases. Again, this may be due to poor statistics, unequal particle sizes and preferred orientation effects in the measured data. The extensive growth of the intensity of the peaks associated with the $Al_9Ni_{2-x}Fe_x$ ("2") and $Al_3Ni_{1-x}Fe_x$ ("6") at $2\theta = 43.55$ deg ($d = 0.207$ nm) and $Al_9Ni_{2-x}Fe_x$ ("2") at $2\theta = 44.4$ deg ($d = 0.203$ nm) was observed after annealing at 600 °C. This result pointed to the growth and/or coarsening of the $Al_9Ni_{2-x}Fe_x$ phase. The growth of the volume fraction of the $Al_3Ni_{1-x}Fe_x$ phase seems unlikely, since we did not find that phase in the SEM study. The intensity of the peak at $2\theta = 49.4$ deg ($d = 0.184$ nm), associated with the $Al_{11}La_3$ ("3"), $Al_8Fe_{2\text{-}x}Ni_xLa$ ("4") and $Al_3Ni_{1-x}Fe_x$ ("6") phases going down with the temperature growth in the alloy (***I***), might occur due to the eutectoid reaction $Al_8Fe_{2-x}Ni_xLa \rightarrow Al_{11}La_3 + Al_9Ni_{2\text{-}x}Fe_x$ and the invariant reaction $Al + Al_3Ni_{1-x}Fe_x \rightarrow Al_9Ni_{2\text{-}x}Fe_x$.

The intensity of the (220) Al peak at $2\theta = 65.17$ deg ($d = 1.43$ nm) in alloy (***I***) after annealing at 600 °C decreased. Using the SEM data (Table III), we associated that observation with the growth of the volume fraction of the $Al_9Ni_{2-x}Fe_x$ phase. In contrast, we found an enormous growth of that peak intensity in alloy (***II***)

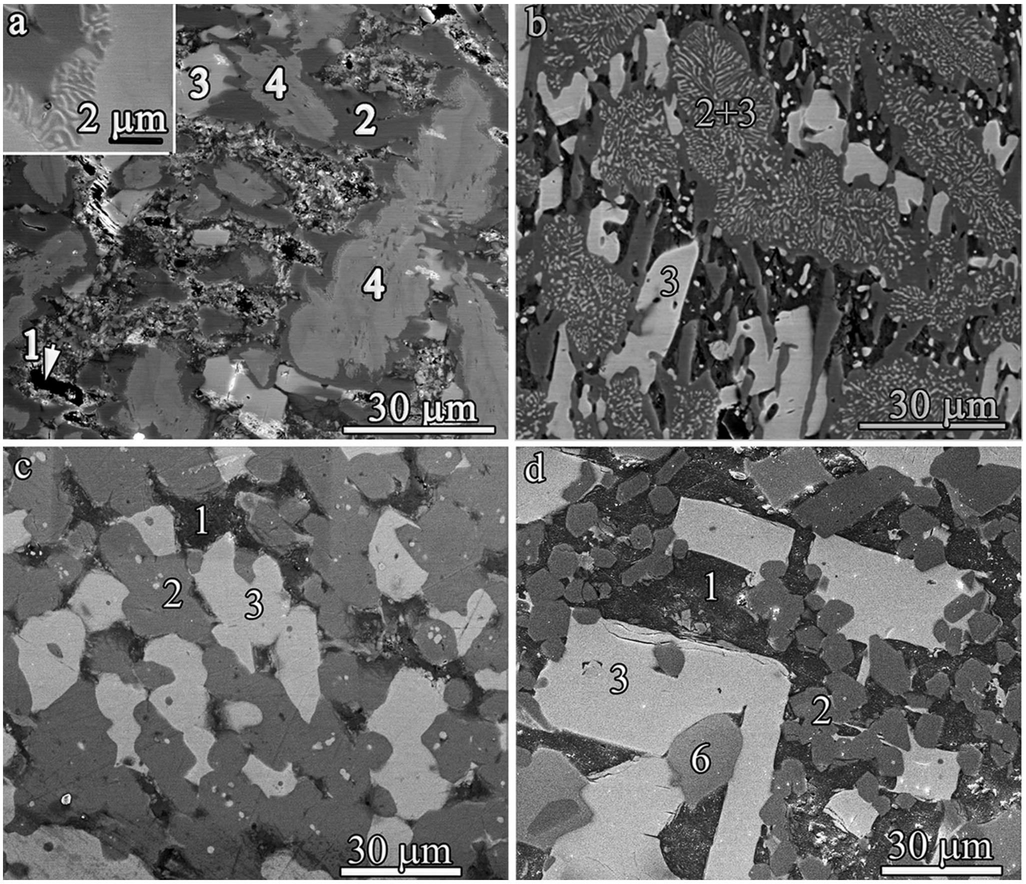

Fig. 12—SE SEM image showing the microstructure after 3 h of annealing at: (*a*) 400 °C for alloy (***I***), with an enlarged image of an $Al_8Fe_{2-x}Ni_xLa$ particle and a eutectic area; (*b*) 500 °C for alloy (***I***); (*c*) 600 °C for alloy (***I***); and (*d*) 600 °C for alloy (***II***). Phases are denoted by 1—Al, 2—$Al_9Ni_{1-x}Fe_x$, 3—$Al_{11}La_3$, 4—$Al_8Fe_{2-x}Ni_xLa$, and 6-$Al_3Ni_{1-x}Fe_x$. The Al-$Al_{11}La_3$-$Al_3Ni_{1-x}Fe_x$ eutectic denoted by "5" in Figs. 2(a) and (b) decomposes.

Table III. Volume Fractions of the Phases Estimated from OM (Before Annealing) and SEM (After Annealing) Data (the Error is ± 10 Pct)

Alloy Phase	$Al_{85}Ni_7Fe_4La_4$ (***I***) Before Annealing	$Al_{85}Ni_7Fe_4La_4$ (***I***) After Annealing 500 °C	600 °C	$Al_{85}Ni_9Fe_2La_4$ (***II***) Before Annealing	$Al_{85}Ni_9Fe_2La_4$ (***II***) After Annealing at 600 °C
Al	16	6	11	20	25
$Al_{11}La_3$	20	37	31	18	32
$Al_9Ni_{2-x}Fe_x$	15	56	58	27	32
$Al_3Ni_{1-x}Fe_x$		—	—		10
$Al_8LaFe_{2-x}Ni_x$	49	—	—	35	—

after annealing at 600 °C, which might arise from the relatively high Al and $Al_3Ni_{1-x}Fe_x$ phase content in the sample (see Table III).

IV. DISCUSSION

To reveal the details of the microstructure formation in two air-cast $Al_{85}Ni_{11-x}Fe_xLa_4$ (where $x = 2$ or 4 at. pct) polycrystalline alloys, which exhibit a number of phases with definite morphologies and different structural defects, we believe that it is important to determine the sequence of phase transformations. The results of the study of two air-cast $Al_{85}Ni_{11-x}Fe_xLa_4$ (where $x = 2$ or 4 at. pct) polycrystalline alloys together with the isothermal annealing of these samples by means of microscopic and microanalysis methods allow us to suggest a number of phase transformation reactions that take place during the cooling of the samples to room temperature in air. In this consideration, we also took

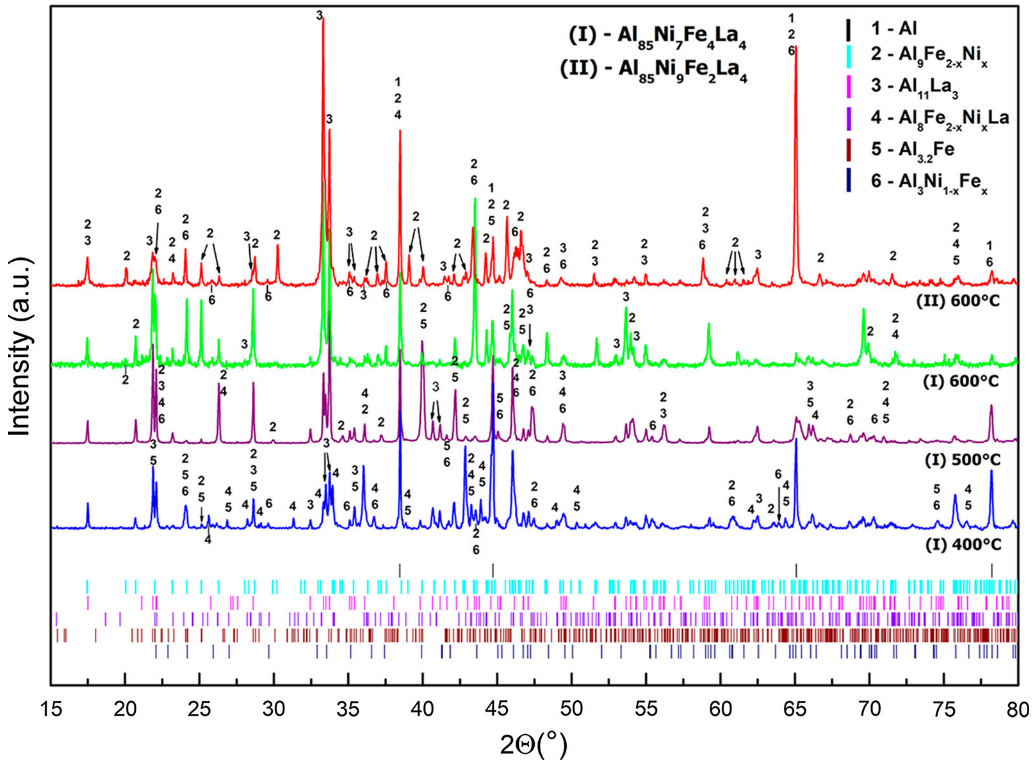

Fig. 13—XRD patterns of the $Al_{85}Ni_7Fe_4La_4$ (***I***) alloy after annealing at 400 °C, 500 °C, and 600 °C and the $Al_{85}Ni_9Fe_{2\ \mathrm{L}}a_4$ (***II***) alloy after annealing at 600 °C.

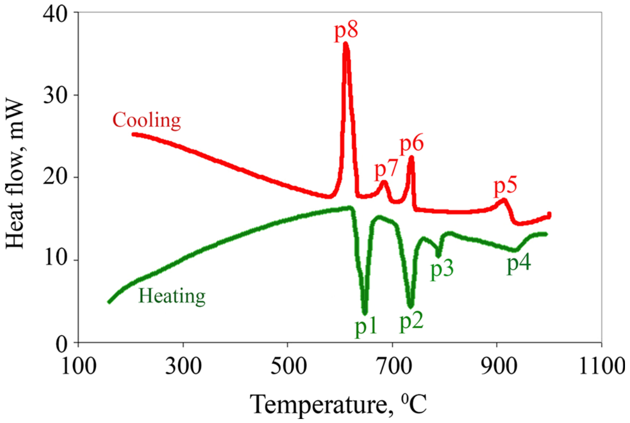

Fig. 14—DSC curves of the Al85Ni7Fe4La4 alloy. Adapted from Ref. [70].

into account the DSC data obtained by our group prior to this investigation[70] for isochronal annealing to temperatures up to 1000 °C with subsequent cooling to room temperature (see Figure 14 and Table IV). As the isothermal annealing experiments demonstrated, the $Al_8LaFe_{2-x}Ni_x$ phase is metastable and undergoes an irreversible eutectoid reaction during heating. Thus, the transformations of the cooled melts in air and the isochronally cooled alloys after heating must be different. The available reference sources were also used to obtain a tentative description of the reaction. Thus, the following phase transformation reactions of the $Al_{85}Ni_{11-x}Fe_xLa_4$ (where $x = 2$ or 4 at. pct) melts are proposed during cooling to room temperature in air:

1. $L \rightarrow L_1 + Al_8Fe_{2-x}Ni_xLa$ primary intermetallic phase solidification
2. $L_1 \rightarrow L_2 + \beta\text{-}Al_{11}La_3$ primary intermetallic phase solidification
3. $\beta\text{-}Al_{11}La_3 + L_2 \rightarrow \alpha\text{-}Al_{11}La_3 + L_2$ phase transformation (invariant reaction)
4. $L_2 + Al_8Fe_{2-x}Ni_xLa \rightarrow L_3 + Al_9Ni_{2-x}Fe_x + Al_{11}La_3$ peritectic reaction
5. $L_3 \rightarrow Al_{11}La_3 + Al_3Ni_{1-x}Fe_x + <Al>$ eutectic reaction

In the studied hypereutectic alloys, an excess of the alloying elements surpassing the eutectic concentration leads to a rapid solidification of primary intermetallic phases in the form of separate particles or their complexes. The growth rate of such primary intermetallic phases is higher than that of the eutectic growth. The solubility limit is < 1 at. pct La for binary Al-La alloys[50] (0.01 at. pct at 640 °C,[50,71]), 1.7 to 2.5 at. pct Fe for Al-Fe alloys,[22] and 1.7 at. pct Ni for Al-Ni alloys (the solid solubility of Ni in Al decreases from 0.11 at. pct at 639.9 °C to 0.01 at. pct at 500 °C). In the course of rapid solidification processing, the enhancement of the solid solubility is observed up to 7.7 at. pct Ni.[72] The growth rates of these primary intermetallic phase particles are much higher than those of the eutectic particles. A close inspection of the OM and SEM images (see Figures 1 and 2) pointed to two scenarios:

A. Solidification of the high-temperature β-$Al_{11}La_3$ phase after the solidification of the $Al_8Fe_{2\text{-}x}Ni_xLa$ phase. This assumption was supported by the SEM observations mentioned above, where relatively large $Al_{11}La_3$ (5 to 20 μm in size) faceted particles surrounded the $Al_8Fe_{2-x}Ni_xLa/Al_9Ni_{2-x}Fe_x$ core shell particles or were located between the $Al_9Ni_{2-x}Fe_x$ particles. The latter particles formed during cooling in a peritectic reaction from the Al_8Fe_{2}_Ni_xLa particles. Thus, two transformations occurred in the first step:

   1. $L \rightarrow L_1 + Al_8Fe_{2-x}Ni_xLa$ primary intermetallic phase solidification followed by
   2. $L_1 \rightarrow L_2 + \beta\text{-}Al_{11}La_3$ primary intermetallic phase solidification

B. The eutectic reaction $L \rightarrow L_1 + Al_8Fe_{2-x}Ni_xLa + \beta\text{-}Al_{11}La_3$. According to Campbell,[65] when an alloy composition departs from the eutectic, or when a third alloying element is present, the interface can become unstable for the same reason as in the case of a simple solid-liquid interface. If one of the phases is faceted, like $Al_{11}La_3$ in our case, the growth of this phase (and consequently the eutectic) is slower at a given undercooling, whereas dendrites ($Al_8Fe_{2-x}Ni_xLa$ particles) may then grow more rapidly than the eutectic at the eutectic composition. The larger $Al_{11}La_3$ particles are faceted, while $Al_8Fe_{2-x}Ni_xLa$ before decomposition adopts a dendritic microstructure; therefore, the described eutectic transformation appears highly likely.

This situation occurred in both alloys, (***I***) and (***II***), but the volume fraction of the $Al_8Fe_{2-x}Ni_xLa$ phase according to our estimate is twice as high (see Table III). The dendrites located on the primary dendritic axis are assemblies of $Al_8Fe_{2-x}Ni_xLa$ particles. The dendritic microstructure forms in the supersaturated solution under unstable temperature and elemental concentration conditions with the influence of crystallographic factors.[73] The dendritic solidification of the $Al_8Fe_{2-x}Ni_xLa$ phase explains the high density of defects found in TEM/STEM-like twins, sharing bands and the formation of the $Al_{3.2}Fe_{1-x}Ni_x$ δ-layers.

Since the $Al_8Fe_{2-x}Ni_xLa$ phase is new and was not thoroughly described, we will discuss the formation of the structural defects in this phase, designated as "1" to "4", in more detail.

The formation of the $Al_{3.2}Fe_{1-x}Ni_x$ δ-layers (defect "1") could be caused by a concentration inhomogeneity in the $Al_8Fe_{2-x}Ni_xLa$ particles. Extended $Al_{3.2}Fe_{1-x}Ni_x$ δ-layers with a flat morphology are associated with layered crystal growth during the crystallization of dendrites from the liquid phase. This type of crystallization was proposed to be a general phenomenon of crystal growth[74] regardless of the composition. If so, an excessive amount of the alloying elements Fe and Ni was dislodged to the liquid/solid interface, and when the critical concentration was reached in the absence of La, an $Al_{3.2}Fe_{1-x}Ni_x$ δ-layer was formed. The density of the $Al_{3.2}Fe_{1-x}Ni_x$ δ-layers in the $Al_8Fe_{2-x}Ni_xLa$ intermetallic compound is relatively high, which is due to the excess content of Fe and Ni and their relatively high diffusion mobility, in comparison with that of La atoms.

The out-of-phase boundary (defect "2") and shifted mirror twins (defects "3" and "4") are associated with dislocations (defects "5") and the $Al_{3.2}Fe_{1-x}Ni_x$ δ-layers (defect "1"). These defects could also form during the dendritic crystallization of the particles. A defect in the atomic arrangement formed by the presence of a dislocation can cause a disturbance of the atomic sequence and thus generate an out-of-phase boundary.[65] In turn, there are several possible reasons for the formation of dislocations. The first is the heterogeneity of the concentration of the elements in the non-equilibrium crystallization of a solid solution of a multicomponent alloy with atomic radii of different sizes, which is quite similar to the formation of $Al_{3.2}Fe_{1-x}Ni_x$ δ-layers. Adjacent layers have somewhat different compositions and parameters of the crystal lattice. At the interfaces of such layers, elastic stresses arise, and when the yield strength is reached, dislocations are formed. The second reason can be the stress at the interface of two phases, namely, the $Al_8Fe_{2-x}Ni_xLa$ and the Al solid solution or the $Al_8Fe_{2-x}Ni_xLa$ and $Al_9Ni_{2-x}Fe_x$. Third, the high density of thermal vacancies could also result in the formation of dislocations.

Twinning (defects "3" and "4") could also appear due to the stress in the particle. However, we cannot confirm that out-of-phase boundaries and twins are generated by dislocations or *vice versa*.

We suppose that the $Al_8Fe_{2-x}Ni_xLa$ phase after the primary solidification forms assemblies of particles along the second (and probably the third) dendritic axis. However, the peritectic reaction "4"

$$L_2 + Al_8Fe_{2-x}Ni_xLa \rightarrow L_3 + Al_9Ni_{2-x}Fe_x + Al_{11}La_3$$

results in a partial dissolution and transformation of $Al_8Fe_{2\text{-}x}Ni_xLa$ to the $Al_9Ni_{2-x}Fe_x$ phase, which is clearly visible in the areas near the surface of the larger $Al_8Fe_{2-x}Ni_xLa$ particles located along the primary dendritic axes, which leads to the formation of core shell structures similar to those described in papers.[75,65] The $Al_8Fe_{2\text{-}x}Ni_xLa$ particles, which are located along the second (third) crystallization axis and are smaller in size, completely transform to $Al_9Ni_{2-x}Fe_x$ particles according to reaction "4". SEM images demonstrated that the $Al_9Ni_{2-x}Fe_x$ particles are elongated in the directions closely perpendicular to the habit plane of the $Al_8Fe_{2-x}Ni_xLa$ particles, which is typical for dendritic crystallization[65] and supports the suggestion of quaternary phase crystallization. The primary crystallization reactions or eutectic reactions described above occur at temperatures higher than 1000 °C and were not observed during the DSC experiment in Reference 70.

In conformity with the binary Al-La phase diagram,[50,76] and the ternary Al-Ni-La phase diagram,[16] the solidification of β-$Al_{11}La_3$ started at the temperature t = 1170 °C and underwent a polymorphic transformation $\beta\text{-}Al_{11}La_3 \rightarrow \alpha\text{-}Al_{11}La_3$ at t = 915 °C. Certainly, minor changes in the crystallization temperature

Table IV. Phase Transformation Temperatures (°C) Upon Isochronous Heating at a Rate of 20 °C/min and Cooling (Same Rate) of the Alloys

	$Al_{85}Ni_7Fe_4La_4$		$Al_{85}Ni_9Fe_2La_4$	
Peaks, see Fig. 17	t_b, °C Peak Beginning	t_{pi}, °C Peak Maximum	t_b, °C Peak Beginning	t_{pi}, °C Peak Maximum
p1	627	647	627	643
p2	712	736	732	746
p3	—	789	—	786
p4	—	933		887
p5	—	913	—	860
p6	743	737	768	749
p7	693	686	—	691
p8	634	612	637	620

may occur in the quaternary system; however, there is unlikely to be a considerable drop in the transformation temperature. Thus, the first peak at t = 913 °C in the DSC curve found by Bakhteeva *et al.*[70] (Figure 14 and Table IV) in the $Al_{85}Ni_7Fe_4La_4$ alloy during cooling (p5) appeared due to the polymorphic transformation β-$Al_{11}La_3 \rightarrow \alpha$-$Al_{11}La_3$ (reaction "3").

The other two peaks, namely, p6 and p7, appearing on the DSC curve during cooling in alloy ***(I)*** (737 °C and 686 °C) or alloy ***(II)*** (749 °C and 691 °C)[70] did not correspond to any known phase transformation in ternary or even binary systems. Several phases were found in the alloys, and they can be considered candidates for a reaction in the temperature range of the p6 and p7 DSC peaks. These phases are $Al_9Fe_{2-x}Ni_x$ and $Al_3Ni_{1-x}Fe_x$. Three reactions for the $Al_9Fe_{2-x}Ni_x$ phase formation may be considered. The first is the peritectic reaction L + $Al_{13}Fe_4$ + $Al_3Ni \rightarrow Al_9Fe_{2-x}Ni_x$. In the ternary Al-Ni-Fe system, this reaction takes place at 809 °C.[19,22,24,29,37] According to Budberg *et al.*,[20] this phase forms in the temperature range of 850 °C and 750 °C. We propose the formation of separate $Al_{13}Fe_4$ particles (isostructural to $Al_{3.2}Fe_{1-x}Ni_x$) at the initial stages of crystallization (observed by Kattner[77] in the binary Al-Fe system at 1160 °C) and Al_3Ni particles in a number of reactions starting from 866 °C.[19,20,22,24,29,37] A high Fe content could decrease the peritectic reaction temperature.[22] The second choice is the peritectic reaction denoted by "4": $L_2 + Al_8Fe_{2-x}Ni_xLa \rightarrow L_3 + Al_9Ni_{2-x}Fe_x + Al_{11}La_3$. The quaternary $Al_8Fe_{2-x}Ni_xLa$ phase was unknown and was not considered in the literature, and this reaction might correspond to one of the peaks. However, the $Al_8Fe_{2-x}Ni_xLa$ phase is metastable and could decompose completely upon heating up to 1000 °C in the DSC experiment. We observed this effect after isothermal heating at 600 °C for 3 hours. Therefore, if the $Al_8Fe_{2-x}Ni_xLa$ particles were not decomposed completely during the DSC heating cycle, then the p6 or p7 peak could appear due to this peritectic reaction. The third possible path of the $Al_9Ni_{2-x}Fe_x$ phase formation might be the transition reaction U:L + $Al_{13}Fe_4 \rightarrow Al_9FeNi$ + (Al), which was found at 650 °C in the Al-Fe-Ni ternary system.[22,23,24] The high volume fraction of the $Al_9Fe_{2-x}Ni_x$ phase found in alloys *I* and *II* after the 600 °C annealing may prove one of these suggestions.

The last scenario is the crystallization of proeutectic Al followed by the eutectic reaction $L_3 \rightarrow Al_{11}La_3 + Al_3Ni_{1-x}Fe_x + \langle Al \rangle$. The crystallization of proeutectic Al seems very likely because we observed bubble-like Al grains (see Figure 2(b)) adjacent to the $Al_9Fe_{2-x}Ni_x$ particles that crowd out the Al-$Al_{11}La_3$-$Al_3Ni_{1-x}Fe_x$ eutectics. These reactions might be responsible for the p7 and p8 peaks (Figure 14) at 612 and 620 °C for alloys ***(I)*** and ***(II)***, respectively. The eutectic reaction resulted in the formation of three phases $L_3 \rightarrow Al_{11}La_3 + Al_3Ni_{1-x}Fe_x + \langle Al \rangle$ (denoted above by "5"), starting at a temperature of 634 °C, which is close to the 625 °C found in the study of Godecke *et al.*[15] and mentioned by Raghavan[16] for Al-Ni-La systems.

Upon the isochronal annealing of the $Al_{85}Ni_7Fe_4La_4$ alloy up to 1000 °C with a constant rate of 20 °C/min, the DSC scans also showed four peaks with a complicated shape[70] (Figure 14, Table IV). However, the intensity and shape of the peaks (p1-p4 in Figure 14) differed from those of the peaks that appeared during cooling (p5-p8), which clearly indicated a diversity of reactions during the heating and cooling of the sample in the same temperature range.

The first endothermic effect (p1) was found in the temperature range between 627 °C and 675 °C, with the peak maximum at $t_{\text{п}1}$ = 647 °C. The complicated shape of the peak with a shoulder in the low-temperature part pointed to numerous reactions. The lowest melting temperature phases are an Al solid solution and an Al/$Al_{11}La_3$/$Al_3Ni_{1-x}Fe_x$ eutectic,[22,76,78] which melt in this temperature range.

In the temperature range from 712 to 800 °C, two overlapping endothermic peaks of a complex shape were observed.

An SEM study of the air-cast alloys after annealing at 400 °C for 3 hours (Figure 12(a) showed that the eutectic colonies designated by "5" in Figure 2(b) in the air-cast sample disappeared, but finely dispersed $Al_{11}La_3$ grains were still noticeable in the areas of the assumed location of the eutectic, which indicates that the thermally activated dissolution reaction does not end in the process of isothermal annealing, which is probably due to insufficient annealing time. In the same sample at the edges of the interface regions of the $Al_8Fe_{2-x}Ni_xLa$ phase, the onset of the eutectoid reaction $Al_8Fe_{2-x}Ni_xLa \rightarrow Al_{11}La_3 + Al_9Ni_{2-x}Fe_x$ is noticeable (Figure 12(a), inset). Isothermal annealing at 500 °C for 3 hours leads to the completion of this reaction (Figure 12(b)). Based on these data, we may assume that the second intense peak (p2) on the DSC curve detected in the temperature range 712 °C to 736 °C[70] can be due to this reaction. Again, these results confirm the metastable nature of the $Al_8Fe_{2-x}Ni_xLa$ phase.

The third peak on the DSC curve (p3) observed upon the heating of this alloy is due to reactions occurring in the temperature range from ~ 750 °C to 789 °C. The nature of this peak could be linked to the transformation of the $Al_9Ni_{2-x}Fe_x$ phase, since it was found at 750 °C but not at 850 °C,[19,22]

The observed fourth peak, $T_{p4} = 933$ °C, could correspond to a polymorphic transformation of the α-$Al_{11}La_3 \rightarrow \beta$-$Al_{11}La_3$ phase transition. Interestingly, there is a relatively strong difference in the temperatures corresponding to the fourth peaks in alloys ***(I)*** and ***(II)***, which were 933 °C and 877 °C, respectively. However, the phase diagram in papers[15,16] shows that the β-α transformation takes place due to the peritectic reaction, and the transformation temperature depends on the Ni content: a higher Ni content, as found in alloy ***(II)***, decreases the transformation temperature.

The DSC spectra of the $Al_{85}Ni_9Fe_2La_4$ alloy (***II***) are similar to those described above, with four endothermic and four exothermic peaks during heating and cooling, respectively. The peaks corresponding to the beginning of the Al melting in both cases ($t = 627$ °C) are related to the close chemical compositions of alloys (***I***) and (***II***). The decrease in the Al content in alloy (***II***) after annealing at 600 °C results in the formation of the $Al_3Ni_{1-x}Fe_x$ phase together with $Al_9Fe_{2-x}Ni_x$, which is visible in Figures 12(c) and (d). The reaction $L + Al_9Fe_{2-x}Ni_x \rightarrow Al_3Ni_{1-x}Fe_x + Al_{11}La$ in alloy (***II***) causes an increase in the volume fraction of the $Al_3Ni_{1-x}Fe_x$ phase after annealing at 600 °C.

V. CONCLUSION

Complex microstructural investigations of two Al alloys, namely, $Al_{85}Ni_{11-x}Fe_xLa_4$ ($x = 2$ or 4 at. pct), were carried out by means of electron and optical microscopy, EDXS, and XRD. These alloys contain several phases, including fcc-Al, $Al_{11}La_3$, $Al_3Ni_{1-x}Fe_x$, $Al_9Ni_{2-x}Fe_x$, $Al_8Fe_{2-x}Ni_xLa$, and $Al_{3.2}Fe_{1-x}Ni_x$, in the form of δ-layers in the $Al_8Fe_{2-x}Ni_xLa$ particles. OM demonstrated that a relatively small difference in the Fe and Ni content in the alloys resulted in a significant increase in the volume fraction of the $Al_9Ni_{2-x}Fe_x$ phase in the Ni-rich $Al_{85}Ni_9Fe_2La_4$ alloy. In contrast, the content of the $Al_8Fe_{2-x}Ni_xLa$ phase is twice as high as that in the $Al_{85}Ni_7Fe_4La_4$ alloy. The microstructure of $Al_8Fe_{2-x}Ni_xLa$ was studied in more detail. In addition to the δ-$Al_{3.2}Fe_{1-x}Ni_x$ inclusions with the habit plane parallel to the ***a***-axis, out-of-phase boundaries caused by the $a/2$ (half unit cell) shift, shifted mirror twins and dislocations were found. A defect with zig-zag contrast appeared due to the overlapping of the shifted mirror twins with the matrix.

The high density of the defects in this phase was caused by the dendritic growth of $Al_8Fe_{2-x}Ni_xLa$ particles. The composition of the quaternary phase measured by EDXS is Al:Fe:Ni:La = 8:1.1:0.9:1. Therefore, the quaternary phase can be described by the general formula $Al_8Fe_{1.1}Ni_{0.9}La$. Heating experiments demonstrated that this phase is metastable and undergoes an irreversible transformation: $Al_8Fe_{2-x}Ni_xLa \rightarrow Al_9Ni_{2-x}Fe_x + Al_{11}La_3$.

The $Al_9Ni_{2-x}Fe_x$ ternary phase contains Ni = 15 ± 1 at. pct and Fe = 3 ± 1 at. pct, and the $Al_3Ni_{1-x}Fe_x$ phase contains Ni = 23.5 ± 1.0 at. pct and Fe = 1.5 ± 1.0 at. pct.

Based on microstructural data and the results obtained under isothermal and isochronous annealing, a sequence of reactions determining the phase composition of the alloys upon cooling and heating was proposed. These reactions are as follows:

1. $L \rightarrow L_1 + Al_8Fe_{2-x}Ni_xLa$ primary intermetallic phase solidification
2. $L_1 \rightarrow L_2 + \beta$-$Al_{11}La_3$ primary intermetallic phase solidification
3. β-$Al_{11}La_3 + L_2 \rightarrow \alpha$-$Al_{11}La_3 + L_2$ phase transformation (invariant reaction)
4. $L_2 + Al_8Fe_{2-x}Ni_xLa \rightarrow L_3 + Al_9Ni_{2-x}Fe_x + Al_{11}La_3$ peritectic reaction
5. $L_3 \rightarrow Al_{11}La_3 + Al_3Ni_{1-x}Fe_x + \langle Al \rangle$ eutectic reaction

The influence of Fe within 2 to 4 at. pct on the phase content was not revealed in the air-cast alloys. However, after isothermal annealing at 600 °C in the alloy containing 4 at. pct Fe, the $Al_3Ni_{1-x}Fe_x$ phase was not found, but in the alloy containing 2 at. pct Fe, this phase is present in the amount of ~ 10 vol pct.

ACKNOWLEDGMENTS

The alloy formation and OM work was carried out under state Assignment No 007-00129-18-00 (IMET RAS). The XRD and EM experiments were supported by the Ministry of Science and Higher Education within the state assignment FSRC “Crystallography and Photonics” RAS. The XRD analysis was performed using the equipment of the Shared Research Center FSRC “Crystallography and Photonics” RAS.

REFERENCES

1. A. Inoue, K. Ohtera, A.-P. Tsai, and T. Masumoto: *Jpn. J. Appl. Phys.*, 1988, vol. 27, pp. L280–82.
2. A. Inoue, K. Ohtera, A.-P. Tsai, H. Kimura, and T. Masumoto: *Jpn. J. Appl. Phys.*, 1988, vol. 27, pp. L1579–82.
3. Y. He, S.J. Poon, and G.J. Shiflet: *Science*, 1988, vol. 241, pp. 1640–42.

4. M.T. Kim, Y. Hwan, and I. Akihisha: *Mater. Trans. JIM*, 1990, vol. 31, pp. 747–49.
5. Y. He, G.M. Dougherty, G.J. Shiflet, and S.J. Poon: *Acta Metall. Mater.*, 1993, vol. 41, pp. 337–43.
6. T. Mika, M. Karolus, G. Haneczok, L. Bednarska, E. Łagiewka, and B. Kotur: *J. Non. Cryst. Solids*, 2008, vol. 354, pp. 3099–3106.
7. M.T. Kim, Y. Hwan, and I. Akihisha: *Mater. Trans. JIM*, 1991, vol. 32, pp. 331–38.
8. H. Chen, Y. He, G.J. Shiflet, and S.J. Poon: *Scr. Metall. Mater.*, 1991, vol. 25, pp. 1421–24.
9. R. Raggio, G. Borzone, and R. Ferro: *Intermetallics*, 2000, vol. 8, pp. 247–57.
10. A.L. Vasiliev, M. Aindow, M.J. Blackburn, and T.J. Watson: *Intermetallics*, 2004, vol. 12, pp. 349–62.
11. A.L. Vasiliev, M. Aindow, M.J. Blackburn, and T.J. Watson: *Intermetallics*, 2005, vol. 13, pp. 741–48.
12. T. Mika and B. Kotur: *Chem. Met. Alloys*, 2010, vol. 3, pp. 208–19.
13. W. Tang, J. Liang, G. Rao, Y. Guo, and Y. Zhao: *J. Alloys Compd.*, 1995, vol. 218, pp. 127–30.
14. V. Raghavan: *J. Phase Equilibria*, 2001, vol. 22, pp. 1995–96.
15. T. Godecke, S. Wensheng, L. Reinhard, and L. Ke: *Zeitschrift für Met.*, 2001, vol. 92, pp. 717–22.
16. V. Raghavan: *J. Phase Equilibria Diffus.*, 2006, vol. 27, p. 392.
17. V.G. Rivlin and G.V. Raynor: *Int. Met. Rev.*, 1980, vol. 3, pp. 79–93.
18. G.V. Raynor and V.G. Rivlin: *Phase Equilibria in Iron Ternary Alloys : A Critical Assessment of the Experimental Literature*, Institute., Institute of Metals North American Publications Center, London, 1988.
19. M. Khaidar, C.H. Allibert, and J. Driole: *Zeitschrift für Met.*, 1982, vol. 73, pp. 432–38.
20. P. Budberg, A. Prince, G. Cacciamani, R. Ferro, B. Grushko, P. Perrot, and R. Schmid-fetzer: in *Ternary Alloys*, G.E. G.Petzow, ed., vol. 1, VCH., VCH, Weinheim, 2004, pp. 329–58.
21. V. Raghavan: *J. Phase Equilibria Diffus.*, 2006, vol. 27, pp. 489–90.
22. L. Eleno, K. Frisk, and A. Schneider: *Intermetallics*, 2006, vol. 14, pp. 1276–90.
23. I. Chumak, K.W. Richter, and H. Ipser: *Intermetallics*, 2007, vol. 15, pp. 1416–24.
24. L. Zhang and Y. Du: *Comput. Coupling Phase Diagrams Thermochem.*, 2007, vol. 31, pp. 529–40.
25. L. Zhang, Y. Du, H. Xu, C. Tang, H. Chen, and W. Zhang: *J. Alloys Compd.*, 2008, vol. 454, pp. 129–35.
26. L. Zhang, J. Wang, Y. Du, R. Hu, P. Nash, X.G. Lu, and C. Jiang: *Acta Mater.*, 2009, vol. 57, pp. 5324–41.
27. A.J. Bradley and A. Taylor: *Philos. Mag. J. Sci.*, 1937, vol. 23, pp. 1049–67.
28. A. Yamamoto and H. Tsubakino: *Scr. Mater.*, 1997, vol. 37, pp. 1721–25.
29. V.I. Dybkov: *J. Mater. Sci.*, 2000, vol. 5, pp. 1729–36.
30. U. Burkhardt, Y. Grin, M. Ellner, and K. Peters: *Acta Crystallogr. Sect. B Struct. Sci.*, 1994, vol. 50, pp. 313–16.
31. K. Schubert, U. Roesler, M. Kluge, K. Anderko, and L. Harle: *Naturwissenschaften*, 1953, vol. 40, p. 437.
32. A.J. Bradley and C.S. Cheng: *Z. Krist.*, 1938, vol. 99, pp. 480–87.
33. C.J. Simensen and R. Vellasamy: *Zeitschrift für Met.*, 1977, vol. 68, pp. 428–31.
34. H.E. Hollingworth, G.R. Frank, and R.E. Willett: *Trans. Met. Soc. AIME*, 1962, vol. 224, p. 188.
35. L.K. Walford: *Acta Crystallogr.*, 1965, vol. 18, pp. 287–91.
36. A.J. Bradley and A. Taylor: *Proc. R Soc. A Math. Phys. Sci.*, 1938, vol. 166, pp. 353–75.
37. A. Schrader and H. Hanemann: *Aluminium*, 1943, vol. 25, pp. 339–42.
38. L.F. Mondolfo: *No Title*, Butterworth, London-Boston, 1976.
39. V. Raghavan: *J. Phase Equilibria*, 1994, vol. 15, pp. 411–13.
40. A.J. Bradley and A. Taylor: *J. Inst. Met*, 1940, vol. 66, pp. 53–65.
41. M. Ellner and T.Z. Rohrer: *Zeitschrift für Met.*, 1990, vol. 81, pp. 847–49.
42. A. Tsai, A. Inoue, and T. Masumoto: *Mater. Trans. JIM*, 1989, vol. 30, pp. 463–73.
43. U. Lemmerz, B. Grushko, C. Freiburg, and M. Jansen: *Philos. Magn. Lett.*, 1994, vol. 69, pp. 141–46.
44. B. Grushko and K. Urban: *Philos. Magn. Part B*, 1994, vol. 70, pp. 1063–75.
45. M. Döblinger, R. Wittmann, and B. Grushko: *J. Alloys Compd.*, 2003, vol. 360, pp. 162–67.
46. Z.H. Huang, J.F. Li, Q.L. Rao, and Y.H. Zhou: *Intermetallics*, 2007, vol. 15, pp. 1139–46.
47. Y.S. Kim, J.S. Nguen, O.T.H. Choi, P.P. Kim, and J.C. Kwon: *Chem. Sustain. Dev.*, 2007, vol. 15, pp. 175–79.
48. A.H. Gomes de Mesquita and K.H.J. Buschow: *Acta Crystallogr.*, 1967, vol. 22, pp. 497–501.
49. K.H.J. Buschow: *Philips Res. Rep.*, 1965, vol. 20, pp. 337–48.
50. K.A. Gschneidner and F.W. Calderwood: *Bull. Alloy Phase Diagr.*, 1988, vol. 9, pp. 686–89.
51. I. Tamura, T. Mizushima, Y. Isikawa, and J. Sakurai: *J. Magn. Magn. Mater.*, 2000, vol. 220, pp. 31–38.
52. V.M.T. Thiede, T. Ebel, and J. Wolfgang: *J. Mater. Chem.*, 1998, vol. 8, pp. 125–30.
53. A.L. Vasil'ev, A.G. Ivanova, N.D. Bakhteeva, N.N. Kolobylina, A.S. Orekhov, M.Y. Presnyakov, and E.V. Todorova: *Crystallogr. Rep.*, 2015, vol. 60, pp. 23–29.
54. M.B. Manyako, I.N. Stets, I.V. Kivach, O.S. Zarechnyuk, and T.I. Janson: *Dopovidi Akad. Nauk Ukr. RSR Seriya B Geol. Khimichni ta Biol. Nauk.*, 1983, vol. 1983, pp. 39–41.
55. A. Hull: *Phys. Rev.*, 1917, vol. 10, pp. 661–96.
56. P.J. Black: *Acta Crystallogr.*, 1955, vol. 8, pp. 43–48.
57. J. Grin, U. Burkhardt, M. Ellner, and K. Peters: *Zeitschrift für Krist.*, 1994, vol. 209, pp. 479–87.
58. K. Sugiyama, T. Obata, and K. Hiraga: *Mater. Trans.*, 2012, vol. 8, pp. 1357–62.
59. I.I. Zalutskii and P.I. Kripyakevich: *Kristallografiya*, 1967, vol. 12, pp. 394–97.
60. H. Nowotny: *Zeitschrift fuer Met.*, 1942, vol. 34, pp. 22–24.
61. I.I. Zalutskii and P.I. Kripyakevich: *Dopovidi Akad. Nauk Ukr. RSR, Seriya A Fiz. ta Mat. Nauk.*, 1967, vol. 1967, pp. 362–65.
62. V.M. Thiede, W. Jeitschko, S. Niemann, and T. Ebel: *J. Alloys Compd.*, 1998, vol. 267, pp. 23–31.
63. D. Gout, E. Benbow, O. Gourdon, and G.J. Miller: *Inorg. Chem.*, 2004, vol. 43, pp. 86–90.
64. P.A. Stadelmann: *Ultramicroscopy*, 1987, vol. 21, pp. 131–45.
65. F.C. Campbell: *Phase Diagrams Understanding the Basics*, ASM international, Almere, 2012.
66. M. Zurbuchen, W. Tian, X. Pan, D. Fong, S.K. Streiffer, M.E. Hawley, J. Lettieri, Y. Jia, G. Asayama, S.J. Fulk, D.J. Comstock, and S. Knapp: *J. Mater. Res.*, 2007, vol. 22, pp. 1439–71.
67. A.L. Vasiliev, G. VanTendeloo, S. Amelinckx, Y. Boikov, E. Olsson, and Z.G. Ivanov: *Phys. C-Superconductivity*, 1995, vol. 244, pp. 373–88.
68. C.L. Jia, L. Houben, and K. Urban: *Philos. Magn. Lett.*, 2006, vol. 86, pp. 683–90.
69. A.M.B. Douglas: *Acta Crystallogr.*, 1950, vol. 3, pp. 19–24.
70. N.D. Bakhteeva, E.V. Todorova, N.N. Kolobylina, A.L. Vasil'ev, and V.P. Sirotinkin: *Russ. Metall.*, 2013, vol. 2013, pp. 206–16.
71. M.E. Drits, E.S. Kadaner, and N.D. Shoa: *Russ. Met.*, 1969, vol. 1, pp. 113–17.
72. G. Ghosh: *Landolt-Börnstein: Numerical Data and Functional Relationships in Science and Technology—New Series.*, 2005.
73. A. Kelly and K.M. Knowles: *Crystallography and Crystall Defects*, Wiley, Hoboken, 2012.
74. W.A. Tiller: *J. Appl. Phys.*, 1958, vol. 29, pp. 611–18.
75. V. Voort and W. Baldwin: in *ASM Handbook Volume 9: Metallography and Microstructures*, G.F.V. Voort, ed., ASM International, Novelty, OH, 2004, pp. 152–64.
76. R.P. Elliott and F.A. Shunk: *Bull. Alloy Phase Diagr.*, 1981, vol. 2, pp. 219–21.
77. U.R. Kattner: *Binary Alloy Phase Diagrams*, 2nd ed., ASM International, Metals Park, 1990.
78. M. Singleton, J. Murray, and P. Nash: *Binary Alloy Phase Diagrams*, 2nd ed., ASM International, Metals Park, 1990.